

UNIVERSITY OF POTSDAM

BACHELOR THESIS

Light-induced magnetization dynamics in Nickel under different excitation conditions

Supervisor:

Alexander VON REPPERT

Examiner:

Prof. Dr. Matias BARGHEER

Co-Supervisor:

Dr. Marwan DEB

Co-Examiner:

Dr. Clemens VON KORFF SCHMISING

Author:

Fried-Conrad WEBER

*A thesis submitted in fulfillment of the requirements
for the degree of Bachelor of Science*

Ultrafast Dynamics in Condensed Matter group
Institute of Physics and Astronomy

November 7, 2021

UNIVERSITY OF POTSDAM

*Abstract*Faculty of Science
Institute of Physics and Astronomy

Bachelor of Science

Light-induced magnetization dynamics in Nickel under different excitation conditions

by Fried-Conrad WEBER

Diese Arbeit behandelt die Messung der zeitaufgelösten Magnetisierung von einem 20nm und einem 200nm Nickel Film. Die 200nm Probe wird dabei unter 2 verschiedenen Geometrien angeregt. Zum einen von der Vorderseite und zum anderen von der Rückseite. Ziel ist es, die Abhängigkeit der Magnetisierungsdynamik vom externen Magnetfeld sowie der Fluenz zu bestimmen. Neben der Demagnetisierung und Remagnetisierung werden auch andere Aspekte untersucht. So wird die Präzession der Magnetisierung als auch die magneto-akustische Dynamik untersucht, welche in der Arbeitsgruppe mittels Röntgen-diffraktion gemessen wurden. Zur theoretischen Beschreibung der Proben wird die Python Bibliothek *udkm1Dsim* genutzt. Diese ist in der Lage, neben der Magnetisierungsdynamik auch Schallwellen in der Probe zu simulieren.

This thesis discusses the time-resolved magnetization of a 20nm and 200nm nickel film. The 200nm sample is measured in two different geometries. These are front side pumping and backside pumping. The fluence dependency, as well as the dependency of the external field, are measured. Aside from demagnetization and remagnetization, other aspects such as the precession of the magnetization are investigated. Also, the magneto-acoustic dynamics are studied, which were measured in the UDKM-group by ultrafast X-ray diffraction. The theoretical description of the samples is done by using the python library *udkm1Dsim*. It can be used to simulate the magnetization dynamics as well as strain pulses.

Contents

Abstract	iii
1 Introduction	1
2 Theoretical background	3
2.1 Magneto-optic Kerr effect	3
2.2 N-Temperature models	4
2.2.1 Three temperature model	4
2.2.2 Microscopic three temperature model	5
2.3 Landau-Lifschitz-Gilbert equation	7
3 Experimental results	11
3.1 Experimental Setup	11
3.1.1 Beamprofile	12
3.1.2 Characterization of the electro-magnet	13
3.1.3 Samples	14
3.1.4 Data analysis procedure	16
3.2 Front side excitation of the 20nm sample	19
3.3 Front side excitation of the 200nm sample	21
3.3.1 Excitation fluence series for 200nm Nickel	21
3.3.2 B-field series for 200nm Nickel	22
3.4 Backside excitation of the 200nm sample	23
3.4.1 B-field series for 200nm Nickel	23
3.4.2 Excitation fluence series for 200nm Nickel	24
4 Discussion of the results	25
4.1 Magnetization dynamics	25
4.1.1 Demagnetization by direct excitation.	26
4.1.2 Demagnetization by indirect excitation	32
4.2 Analysis of the magnetization precession	34
4.3 Analysis of the strain response	36
5 Conclusion	39
5.1 Summary	39
5.2 Outlook	40
Bibliography	41
Declaration of Authorship	45

List of Figures

2.1	Three different MOKE geometries	3
2.2	Change of magnetization in microscopic three temperature model	6
2.3	Temperature dependent magnetization according to the Microscopic three temperature model	7
2.4	Magnetisation dynamics governed by the LLG equation	9
2.5	Magnetisation dynamics for different external fields	9
3.1	Pump Probe trMOKE Setup	12
3.2	Beamprofile for frontside excitation for pump and probe	13
3.3	Current dependence of the external B-Field	14
3.4	Absorption profile of the samples	15
3.5	Static hysteresis	16
3.6	Raw data of a trMOKE measurement	17
3.7	Raw data added and subtracted	18
3.8	Relative time-dependent magnetization magnetization change for a 200nm Ni sample	19
3.9	Excitation fluence series for 20nm at B = 180mT	20
3.10	Excitation fluence series for 20nm at B = 640mT	20
3.11	Excitation fluence series for 200nm at B = 180mT	21
3.12	Excitation fluence series for 200nm at B = 640mT	22
3.13	B-field series for 200nm	22
3.14	B-field series for 200nm at $F = 24.2 \frac{\text{mJ}}{\text{cm}^2}$	23
3.15	Excitation fluence series for 200nm at B = 650mT	24
4.1	Comparison of the two magnetization models for 20nm Nickel	27
4.2	Simulated magnetization response upon direct excitation for the 20nm Nickel sample.	28
4.3	Comparison of the two magnetization models for 200nm Nickel	30
4.4	Simulated magnetization response upon direct excitation for the 200nm Nickel sample.	31
4.5	Sample structure for M-Model simulation	32
4.6	Simulated magnetization response upon indirect excitation for the 200nm Nickel sample.	33
4.7	Analyzation of precession for 200nm Nickel front side pumping	34
4.8	Analyzation of precession for 200nm Nickel backside pumping	35
4.9	Analyzation of strain dynamics for 200nm Nickel backside pumping	36
4.10	Qualitative simulation of the shape of the strain pulse.	37
4.11	Strain and magnetization dynamics for 20nm Nickel at $F = 7\text{mJ}/\text{cm}^2$	38

List of Tables

3.1	Conversion factor between power and fluence	13
4.1	List of the simulation parameters	26

List of Abbreviations

fwhm	Full width half m aximum
LLG	Landau–Lifshitz–Gilbert
MOKE	m agneto- o ptic K err e ffect
3TM	T hree temperature m odel
m3TM	M icroscopic t hree temperature m odel
PXS	Plasma x-ray source
trMOKE	time resolved m agneto- o ptic K err e ffect
UXRD	Ultrafast x-ray d iffraction

Physical Constants

Speed of Light	$c_0 = 2.997\,924\,58 \times 10^8 \text{ m s}^{-1}$ (exact)
Planck constant	$h = 6.626\,070\,15 \times 10^{-34} \text{ J s}$ (exact)
Landé-factor for electron	$g_e = 2$ (approximately)
Bohr magneton	$\mu_B = 9.274\,010\,078\,3(28) \times 10^{-24} \text{ J T}^{-1}$
Vacuum permeability	$\mu_0 = 1.256\,637\,062\,12(19) \times 10^{-6} \text{ N A}^{-2}$
Vacuum permittivity	$\epsilon_0 = 8.854\,187\,812\,8(13) \times 10^{-12} \text{ A s V}^{-1} \text{ m}^{-1}$

List of Symbols

<i>A</i>	area	m^2
<i>B</i>	magnetic flux density	$\text{T} (\text{kg A}^{-1} \text{s}^{-2})$
<i>C</i>	heat capacity	$\text{J kg}^{-1} \text{K}^{-1}$
<i>E</i>	energy	J
<i>F</i>	fluence	J m^{-2}
<i>H</i>	magnetic field strength	A m^{-1}
<i>P</i>	power	$\text{W} (\text{J s}^{-1})$
<i>T</i>	temperature	K

Chapter 1

Introduction

The occurrence of long-range magnetic order effects at room temperature is both useful and fascinating. It is useful because, for more than 100 years, it has been utilized to store information. First in the form of wire recording, then as magnetic tapes, and nowadays as hard drives with a lifespan of more than ten years. It is fascinating since already Niels Bohr in 1911 and Hendrika Johanna van Leeuwen in 1919 independently showed in their Ph.D. thesis that classical statistical mechanics cannot rationalize the occurrence of magnetism, which is now known as Bohr-van Leeuwen theorem [1]. This thesis focuses on the magnetization dynamics on ultrafast timescales, namely demagnetization and precession. Here, Ultrafast means that the dynamics are investigated on the picosecond timescale.

Ultrafast magnetization dynamics is an exceptionally interesting research topic. On a fundamental level, the effects of ultrafast coupling between light and matter are of great importance, although it is far from our everyday experience. A broad industry, from laser to computer technology, relies on understanding this kind of interaction. Since the UDKM-group has great experience measuring strain dynamics, the interaction of strain and magnetization is the subject of this thesis. Plausible influences of the strain system on the magnetization are phonons acting as an energy reservoir [2] [3]. Also, the temperature of the phonon system might change the magnetocrystalline anisotropy [4]. In addition, the strain pulses can trigger magnetic precession. For the UDKM-group, measuring ultrafast magnetization dynamics under different excitation scenarios acts as a preparation to measure it simultaneously with ultrafast x-ray diffraction (UXRD). This allows one to measure the magnetization and strain dynamics at the same time.

Aside from that, the magnetization dynamics can be modeled using the `udkm1Dsim` toolbox. Modeling the behavior of the sample allows one to compare different models that explain demagnetization on ultrafast timescales. Also, one can test where the models match the measurements and where the models reach their limit.

In the past, many experiments were done in this field of research. In this paragraph, a short overview of essential concepts is given. In order to model magnetization dynamics, it is helpful to reduce the solid to three sub-systems, lattice, electrons, and spins/magnetization, to handle its complexity. The lattice system is composed of atoms and their vibrational modes. The electrons are charge carriers in metals, which travel at high velocities. Furthermore, the third system, the spins, act like tiny bar magnets, giving Nickel its ferromagnetic properties. All the sub-systems interact with each other and govern the behavior of the whole system. The interaction of these sub-systems is proposed in two different ways. In 1996 a conceptually simple, purely thermodynamic model was published by Beaurepaire et al. [2]. Another more complicated model by Koopmans et al. [3] that relies on quantum mechanics also describes the interaction. Since both models cannot fully describe the magnetization dynamics, it is interesting to ask what they can describe and what not.

Studying this can be achieved by changing the sample and the geometry of the experiment. By doing this, one can compare different mechanisms that lead to demagnetization. One way of demagnetization is described as heating the spin system [2]. Here the pump and

probe come from the same side. The electrons are heated by the pump beam and then exchange energy with the other sub-systems, leading to demagnetization. This explanation is relatively simple but neglects the direct interaction and only relies on thermodynamics. Qualitatively, there are different mechanisms discussed that lead to demagnetization. One is the Elliott–Yafet electron-phonon spin-flip scattering. In this mechanism, an electron is scattered under the emission of a phonon taking over angular momentum [3]. By doing this, the electron flips its spin. Other mechanisms are the electron–magnon spin-flip scattering and Coulomb exchange spin-flip scattering. Also, "the transport of laser-excited non-spin-polarized electrons into the ferromagnet" [5] is discussed. By changing the setup's geometry or the sample itself, one can weaken or strengthen those different mechanisms to study them isolated from another. One, to this point, not well studied type of demagnetization occurs via heat transport. This type can be investigated by pumping a sample from one side and measure from the other. By doing this, the heat is transported via phonons and electrons and leads to a demagnetization. This type of demagnetization has the potential to measure the effects of the different phenomena mentioned above. For example, by inserting an insulating layer, one can impede the transport of electrons.

Ever since the groundbreaking work by Beaurepaire et al., Nickel has served as a model system for ultrafast demagnetization studies in metals. This is due to the fact that it has a Curie temperature of $T_C = 632\text{K}$, significantly above room temperature, and shows a strong demagnetization upon laser excitation in comparison to iron and cobalt [6]. In addition, the well-known thermophysical properties of this material render Nickel an ideal candidate for combined studies of its magnetization and lattice dynamics. Studies of the lattice dynamics have already been conducted in the UDKM-group [7] [8], but the magnetization dynamics have so far not been addressed.

This work helps close this gap and aims to proceed one step towards combined studies of the magnetization and lattice dynamics in the same setup under identical excitation conditions. This can provide experimental data for testing established models for the spin-lattice interactions.

For this thesis, two different nickel films are measured under different excitation conditions. A broad range of fluences is used to excite the material, to test the models at their limits. UXRd measurements done in the UDKM-group with the same samples that yield the strain dynamics are also presented. Using the `udkm1Dsim`-toolbox, the results are compared with simulations of the magnetization and strain dynamics.

This thesis is structured as follows: The theoretical framework to understand and interpret the measurements is given in the second chapter. It contains background information on the MOKE effect that is used to measure the magnetization and established models for the description of ultrafast demagnetization and magnetization precession. In the subsequent chapter, the experimental basics are discussed. Chapter three presents the experimental setup, the samples and results. In the fourth chapter, this behavior is discussed in detail using the models from chapter 2. Experimental data are compared with simulations, and other measurements done in the UDKM-group are taken into consideration. Finally, in the last chapter, the results are evaluated. Also, questions that arise from the experiments are formulated into ideas for future investigations.

Chapter 2

Theoretical background

The following chapter discusses the theoretical framework needed to describe the experiment. In the first section, the magneto-optic Kerr effect is analyzed. This effect is used to measure the relative magnetization of the sample. Afterward, two models that explain the time evolution of the magnetization are shown. These models describe the magnetization by reducing the degrees of freedom in a solid to only three coupled sub-systems representing electron excitations, phonons, and magnetic excitations. The presented three temperature model (3TM) and the microscopic three temperature model (m3TM) describe the main aspects of the de- and remagnetization behavior but do not cover the coherent magnetization precession. The main ingredient to rationalize the observable magnetization precession is the Landau-Lifshitz Gilbert equation presented and derived at the end of this section.

2.1 Magneto-optic Kerr effect

Michael Faraday first discovered the interaction of magnetization and light in the year 1845 [9]. In his experiment, Faraday measured how the polarization of linearly polarized light is rotated while passing through a media inside a magnetic field. Twenty-one years later, John Kerr described a similar effect for reflection [10]. This effect is called the magneto-optic Kerr effect (MOKE). The MOKE is a reliable tool to measure the "surface magnetization of thin films" [11]. In this section, a short description of the MOKE effect is given. One can distinguish three different cases, that are shown in figure 2.1.

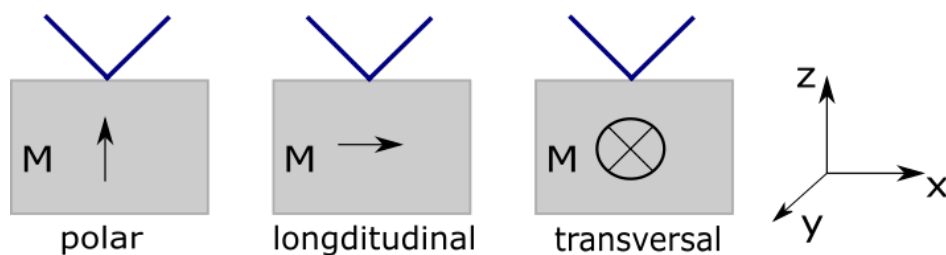


FIGURE 2.1: **Three different MOKE geometries** The probe is indicated via the blue line. The coordinate system on the right is used for the derivation.

In this thesis, the polar MOKE geometry was used to measure the magnetization dynamics.

Linear polarized light is a superposition of right circular polarized (rcp) light and left circular polarized (lcp) light. When the linear polarized light gets reflected on a sample with no magnetization, the lcp and rcp light are reflected such that the polarization of the incident and outgoing beam are the same. However, if the sample is magnetized, the permittivity and, therefore, the refractive index for lcp and rcp are different. The result is that both

components get reflected differently and do not add up with the same polarization as the incident beam. A detailed description can be found in the Ph.D. Thesis of Lisa Willig. [12]

2.2 N-Temperature models

An easy type of model to explain the ultrafast processes in Nickel are N-temperature models. N-Temperature models are easy to calculate but are based on assumptions that are not always suitable. One disadvantage is that N-temperature models assume that each subsystem has a temperature after the excitation. That is not true since the occupation of quantum states may not be describable via Bose-Einstein or Fermi-Dirac statistics. Second, domain effects are neglected. And third, the vectorial character of the magnetization is not described in this model and therefore would not predict precession. Keeping this in mind in the following two different N-temperature models are motivated.

Since the electron- and lattice temperature influence the magnetization behavior, both should be included in the model. In the following, two different models are presented and discussed. First, the model proposed in the groundbreaking paper by Beaurepaire et al. [2], which first shows subpicosecond demagnetization. It expanded a two-temperature model by attributing a temperature to the spins and yields qualitatively good results. Thus it is called the *Three temperature model*. The spins can interchange energy with the electron and the lattice system. The change in spin temperature leads to a change in magnetization.

The second model was published 13 years later [3]. In this model, the electrons and lattice system interact via a more sophisticated model with the magnetization derived from equations of quantum mechanics. This *Microscopic three temperature model* shows two different kinds of demagnetization, depending on the input power, that matches with experiments. [13]

2.2.1 Three temperature model

The three temperature model is motivated by measuring the remanence of Nickel after the excitation with a „60fs pulse coming from a 620nm colliding pulse mode-locked dye laser“ [2]. It is an intuitive approach to map the transient magnetization change to a spin temperature via the static, temperature-dependent magnetization curve $M(T)$ that can be derived using molecular field theory [14]. From that perspective, extending the two-temperature model that is frequently used to describe effects in laser-excited metals to a three-temperature model that incorporates the spin degrees of freedom is straightforward. However, this model needs to be taken with great care because the occupation probabilities assume a thermal distribution after a considerable time, such that a temperature can be assigned. Also, the mode-dependent couplings are not taken into account, and it does not have a predictive power since the coupling constants G_{sl} and G_{se} are phenomenological fitting parameters that are not known from ab-initio theory. Keeping this in mind, the local evolution of all three systems are described by this set of coupled differential equations:

$$\frac{dT_e}{dt} = -\frac{G_{el}}{C_e}(T_e - T_l) - \frac{G_{es}}{C_e}(T_e - T_s) + \frac{P(t)}{C_e}, \quad (2.1)$$

$$\frac{dT_s}{dt} = -\frac{G_{es}}{C_s}(T_s - T_e) - \frac{G_{sl}}{C_s}(T_s - T_l), \quad (2.2)$$

$$\frac{dT_l}{dt} = -\frac{G_{el}}{C_l}(T_l - T_e) - \frac{G_{sl}}{C_l}(T_l - T_s), \quad (2.3)$$

where e is assigned to electrons, l to the lattice, and s to the spins. The phenomenological coupling constants G describe the coupling between the sub-systems. For this Bachelor thesis a temperature gradient may need to be taken into account. This can be achieved by expanding the equations 2.1-2.3 according to Puddel et al [7]:

$$\frac{dT_e}{dt} = \frac{\partial}{\partial z} \left(\kappa_e \frac{\partial T_e}{\partial z} \right) - \frac{G_{el}}{C_e} (T_e - T_l) - \frac{G_{es}}{C_e} (T_e - T_s) + \frac{P(t)}{C_e}, \quad (2.4)$$

$$\frac{dT_s}{dt} = \frac{\partial}{\partial z} \left(\kappa_s \frac{\partial T_s}{\partial z} \right) - \frac{G_{es}}{C_s} (T_s - T_e) - \frac{G_{sl}}{C_s} (T_s - T_l), \quad (2.5)$$

$$\frac{dT_l}{dt} = \frac{\partial}{\partial z} \left(\kappa_l \frac{\partial T_l}{\partial z} \right) - \frac{G_{el}}{C_l} (T_l - T_e) - \frac{G_{sl}}{C_l} (T_l - T_s), \quad (2.6)$$

where κ is the thermal conductivity. This set of coupled differential equations can be solved numerically using the `udkm1Dsim-toolbox`.

2.2.2 Microscopic three temperature model

The Microscopic three temperature model is a more sophisticated model derived from describing the sub-systems and their interaction via quantum mechanics. The sub-system are a "Fermi sea of spinless electrons with a constant density of states". Also, "a separate spin bath [...] obeying Boltzmann statistics". And a phonon system that is described "by using an Einstein model of identical oscillators obeying Bose-Einstein statistics". Where "a more realistic description of the phonon dispersion, within the Debye model" is included. (Supplementary of [3]). The resulting equation that describes the magnetization dynamics m read as follows:

$$\frac{dT_e}{dt} = -\frac{G_{el}}{C_e} (T_e - T_l) + \frac{P(t)}{C_e}, \quad (2.7)$$

$$\frac{dT_l}{dt} = -\frac{G_{el}}{C_l} (T_l - T_e), \quad (2.8)$$

$$\frac{dm}{dt} = Rm \frac{T_l}{T_C} \left(1 - m \coth \frac{mT_C}{T_e} \right). \quad (2.9)$$

Here, R is a coupling constant. For Nickel, R is $17.2 \frac{1}{\text{ps}}$ and $T_C = 632 \text{ K}$ is the Curie temperature. In figure 2.2 the term in brackets from equation 2.9 is analyzed.

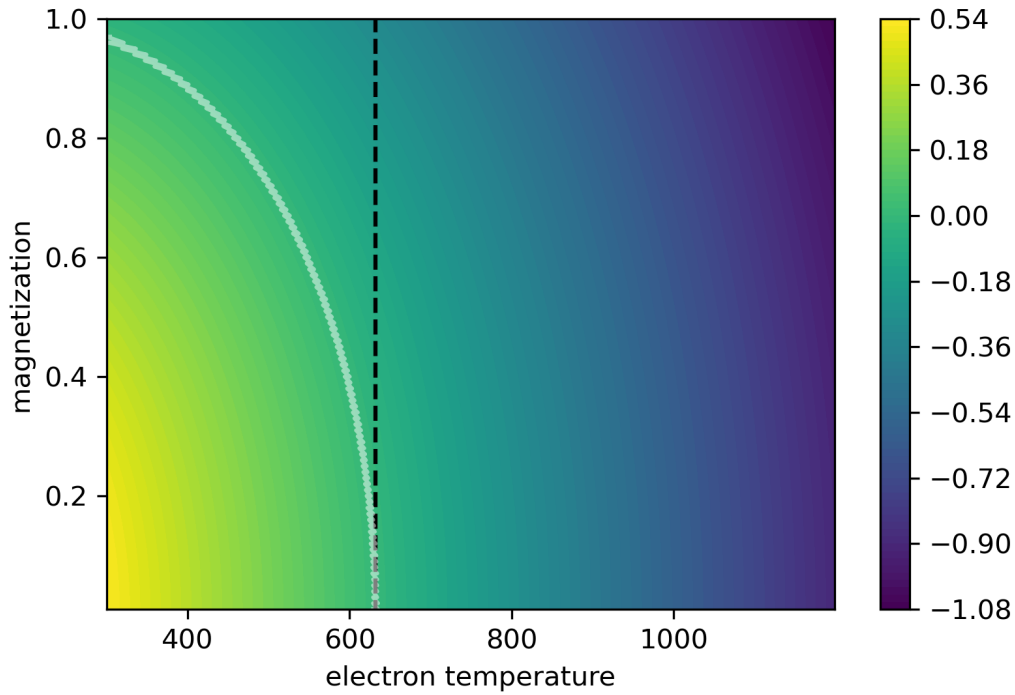


FIGURE 2.2: **Change of magnetization in microscopic three temperature model** The dashed line indicates the Curie temperature. For low magnetization and low temperature the system remagnetizes, for high temperature and high magnetization it demagnetizes. The white line shows, where the change is zero.

At the white line, the derivative of the magnetization is zero. If one assume $T_l = T_e$ this line indicates the magnetization in thermal equilibrium. If $T_l \neq T_e$ the exact value of $\frac{dm}{dT}$ changes, but the sign of the derivative is governed by the bracket in equation 2.9. In figure 2.3 this model is compared to experimental data. [14] (p. 131)

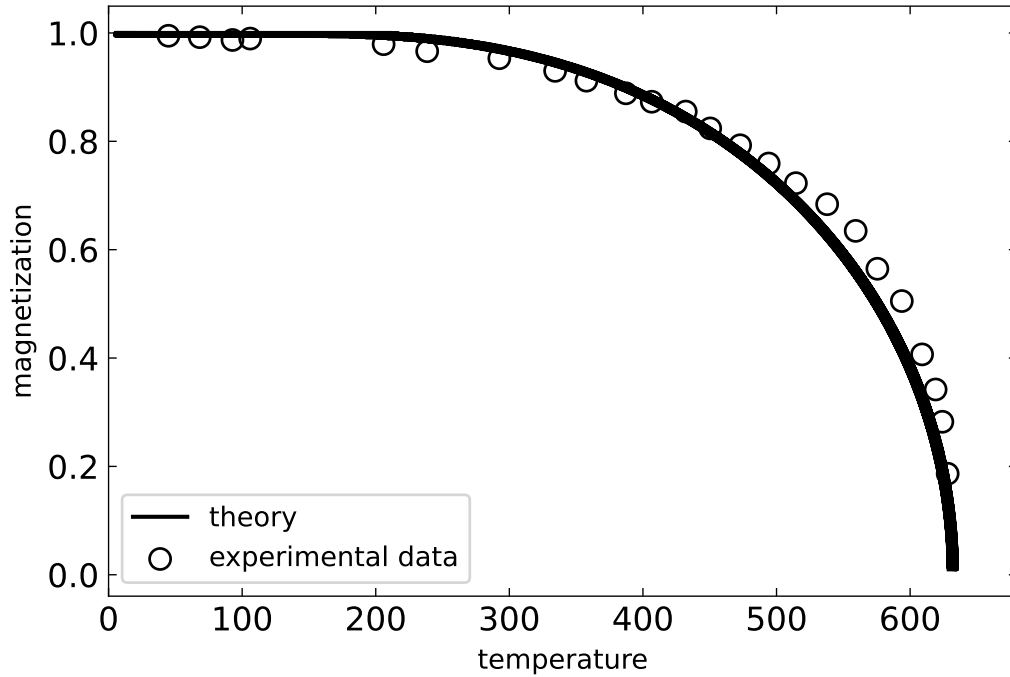


FIGURE 2.3: **Temperature dependent magnetization according to the Microscopic three temperature model** The model matches well with the experimental data

As for the 3TM the model can be expanded to describe the spatial evolution. The equations 2.7-2.9 should then be written as:

$$\frac{dT_e}{dt} = \frac{\partial}{\partial z} \left(\kappa_e \frac{\partial T_e}{\partial z} \right) - \frac{G_{el}}{C_e} (T_e - T_l) + \frac{P(t)}{C_e}, \quad (2.10)$$

$$\frac{dT_l}{dt} = \frac{\partial}{\partial z} \left(\kappa_l \frac{\partial T_l}{\partial z} \right) - \frac{G_{el}}{C_l} (T_l - T_e), \quad (2.11)$$

$$\frac{dm}{dt} = Rm \frac{T_l}{T_C} \left(1 - m \coth \frac{mT_C}{T_e} \right). \quad (2.12)$$

This set of equations shows that the m3TM is not flawless. First, no spatial diffusion of the magnetization is assumed. Furthermore, no energy is transferred into the spin system. The total energy of the system is distributed between the electron- and the lattice sub-system.

2.3 Landau-Lifschitz-Gilbert equation

In this section, a mathematical description of the interaction between spin and the magnetic field is given. The Ehrenfest Theorem, which yields the time evolution of the expectation value of an observable, is needed to describe the magnetization dynamics. The Ehrenfest Theorem [15] for an arbitrary observable \mathcal{O} reads as follows:

$$\partial_t \langle \mathcal{O} \rangle = \frac{i}{\hbar} \langle [\hat{H}, \mathcal{O}] \rangle + \langle \partial_t \mathcal{O} \rangle \quad (2.13)$$

The Hamiltonian can be guessed from the correspondence principle by introducing operators. Using Einsteins sum convention it can be written as:

$$E_{mag} = -\vec{m} \cdot \vec{B} \longrightarrow \hat{H}_{mag} = -\hat{\mu}_j B_j \quad (2.14)$$

If $\hat{\mu}$ is the magnetic dipole moment of an electron, and our observable is the spin, one finds:

$$\partial_t \langle s_i \rangle = -\frac{i}{\hbar} \frac{g_e \mu_B}{\hbar} \langle [s_j B_j, s_i] \rangle \quad (2.15)$$

Using the commutator relation for the spin, this equation can also be written as:

$$\partial_t \langle \vec{s} \rangle = \underbrace{\frac{g_e \mu_B}{\hbar}}_{\gamma} \mu_0 \langle \vec{s} \times \vec{H}_{eff} \rangle \quad (2.16)$$

Here, γ is also called the gyromagnetic ratio. To describe the magnetization, one must add up all contributing spins $M = \sum_i s_i$. This yields the following equation:

$$\partial_t \vec{M} = \gamma \mu_0 \left(\vec{M} \times \vec{H}_{eff} \right) \quad (2.17)$$

This equation only describes the precession of the magnetization. To take damping into consideration, another term has to be added. As for damping in classical mechanics, this term should be proportional to the precession velocity. Since the vector describing the damping should also be perpendicular to the effective magnetic field, it is evident that the revised equation is frequently written as:

$$\partial_t \vec{M} = \gamma \mu_0 \left(\vec{M} \times \vec{H}_{eff} \right) - \frac{\lambda}{M} \left(\vec{M} \times \partial_t \vec{M} \right). \quad (2.18)$$

The effective field is the sum of the external and anisotropy field. This equation is the Landau-Lifshitz-Gilbert equation, which in this form was described by Gilbert in 1955 [16]. In the experiment, the in-plane anisotropy is changed by a pump pulse. Assuming a crystal field anisotropy (assumed to be in-plane) and an out-of-plane external field, the direction of the effective field changes. In figure 2.4 the time evolution for such a scenario is depicted.

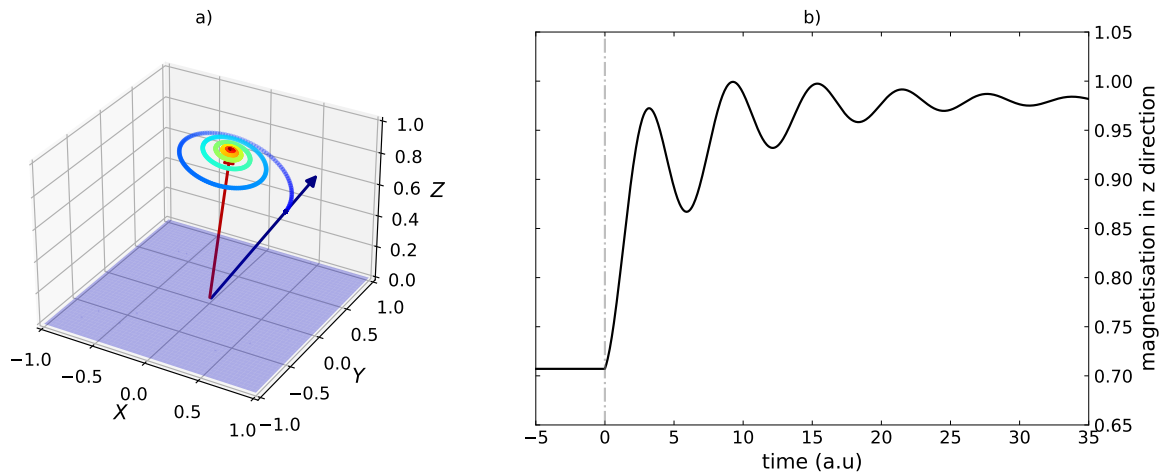


FIGURE 2.4: **Magnetisation dynamics governed by the LLG equation:** a) The blue arrow indicates the direction of the effective field before time zero. The red arrow indicates the direction after time zero. The color indicates the time evolution. The blue surface indicates the orientation of the sample surface. b) The magnetization in the z-direction is plotted against time

This means, by changing the effective field rapidly, it should be possible, to trigger a precession. In figure 2.5 the dynamics for different external fields according this model are plotted. As in figure 2.4 the effective field is modeled as a step at $t = 0$.

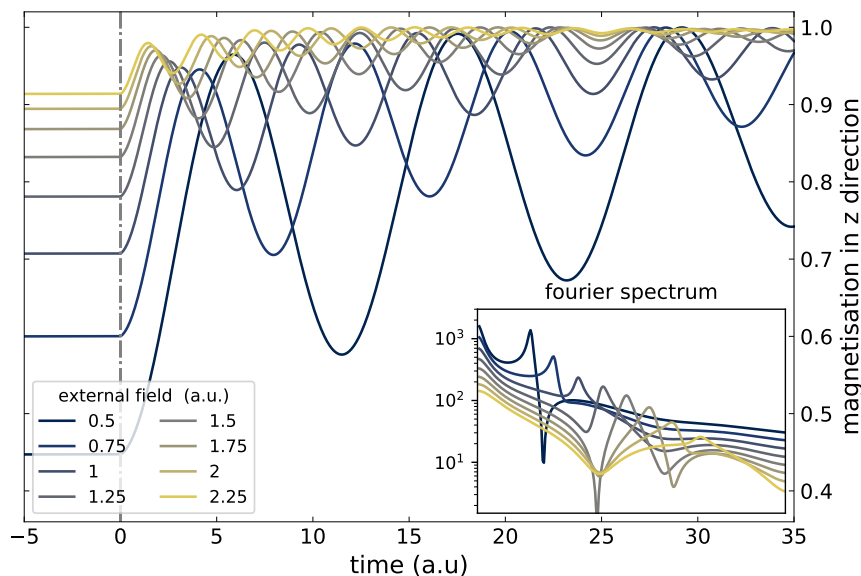


FIGURE 2.5: **Magnetisation dynamics for different external fields** By increasing the external field, the precession frequency increases linear

This model omits demagnetization as discussed in section 2.2. Also, higher-order spin waves are not included. Since the 3-temperature model does not explain the vectorial character of the magnetization dynamics, another model is needed to explain magnetization precession and demagnetization. This is already achieved by expanding the LLG equation into the Landau Lifshitz Bloch equation [17] [18].

Chapter 3

Experimental results

The following chapter discusses the setup and data analysis for the time-resolved MOKE experiments carried out in this thesis. First, an overview of the time-resolved-MOKE setup (trMOKE) is given. In the end, the experimental results for the magnetization response of the samples under direct and for the 200nm sample under indirect excitation conditions are presented. A detailed discussion of the data is deferred to the next chapter.

3.1 Experimental Setup

The experimental setup for time-resolved MOKE experiments under direct excitation has been developed by Lisa Willig in her Ph.D. project [12]. A general sketch of the setup is shown in figure 3.1. An amplified fs-laser system operating at a central wavelength of 800nm and a repetition rate of 1kHz that supplies p-polarized pulses with a duration of approximately 150fs is used to excite and measure the material. The laser beam is then divided into a pump and a probe pulse, using an 80/20 beam splitter such that both pulses are inherently synchronized since they are derived from the same laser. A $\lambda/2$ -plate followed by a polarizer is used to adjust the pump and probe's intensity. The fluence is adjusted by the incident pulse energy and the position of the focusing lens. The frequency of the probe pulse is doubled via second harmonic generation (SHG) in a beta-barium borate (BBO) crystal. The residual pump is filtered out by multiple dichroic mirrors and an infrared absorption filter (Schott BG39). A 15cm long mechanical delay stage is used to change the path length of the pump, to set the relative time delay between pump and probe. A chopper sets the repetition rate of the pump pulse to 500Hz. This allows for a direct comparison of the pumped and unpumped signal probed by a subsequent laser pulse, eliminating signal changes due to the long-term drifts of the laser system.

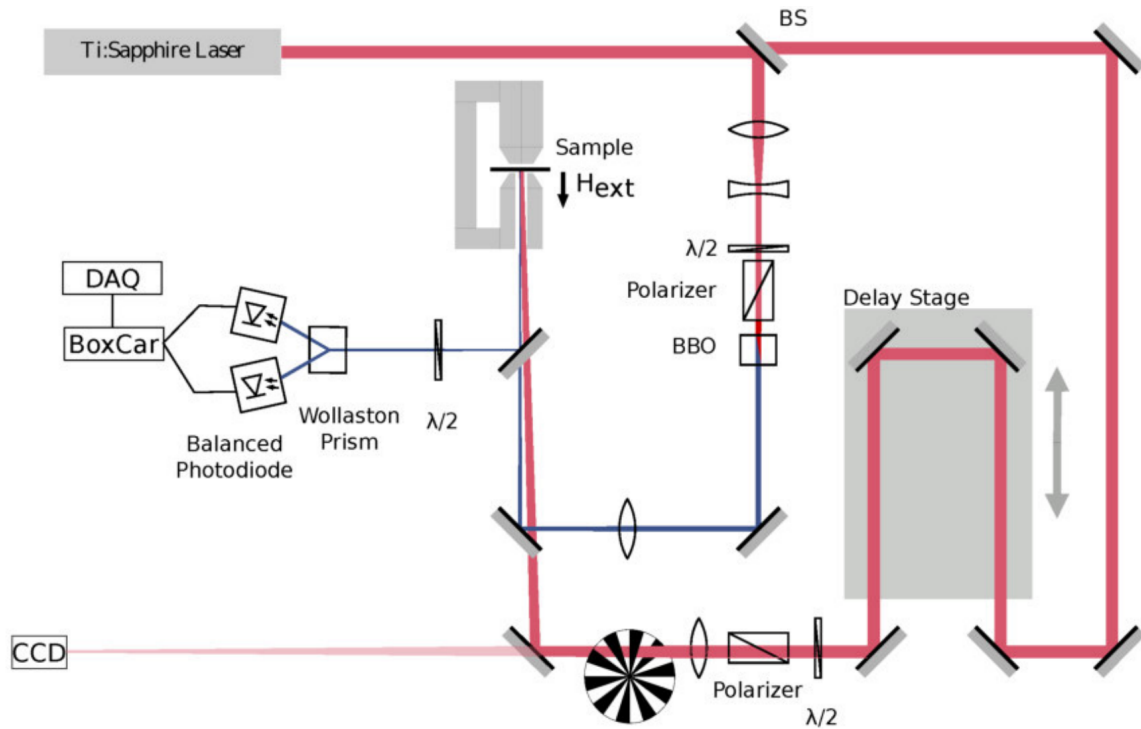


FIGURE 3.1: **Pump Probe trMOKE Setup:** A delayed 800nm pump pulse is used to excite the sample. The Kerr rotation is measured using a 400nm probe and a balanced photodiode [12].

As shown in figure 3.1, the reflected probe passes a $\lambda/2$ -plate and is then separated using a Wollaston prism. With balanced photodiodes, the p- and s- polarized parts are measured. A change in the magnetization results in a rotation of the polarization of the reflected probe light. This is measured as a change of the ratio between the s- and p-polarized light detected in the balanced photodiode. We obtain information on the magnetization dynamics by measuring the B-field dependent, relative change between the p- and s-polarized contributions of the laser light.

In the course of the BSc thesis, together with Marwan Deb and Alexander von Reppert, the setup was extended such that it allows for the excitation of the sample from the backside while keeping the probe geometry fixed. By doing this, one can compare two different types of demagnetization, i.e., direct and indirect excitation. For the front side pumping, this type from now will be called *demagnetization by direct excitation*. And for backside excitation, this will be called *demagnetization by indirect excitation*.

In the following subsections, first the beam profile is analyzed, then the magnet is characterized, and last but not least, the analysis of raw data is shown exemplarily.

3.1.1 Beamprofile

In order to calculate the incident laser fluence, it is crucial to know the size of the excitation beam. Therefore, the beam profile for front and backside excitation is chosen such that the footprint of the excitation spot is much larger than that of the probe spot to probe a homogeneously excited area. The spot size is set by varying the path length between the focussing length and the sample. In the following, the measurement of the beam profile for both setups will be discussed. The goal is to find a way to calculate the fluence of one pulse by measuring the power. The beam profile was measured by inserting a camera at the exact position where the sample is. With the data from the camera, one gets the images shown in figure 3.2.

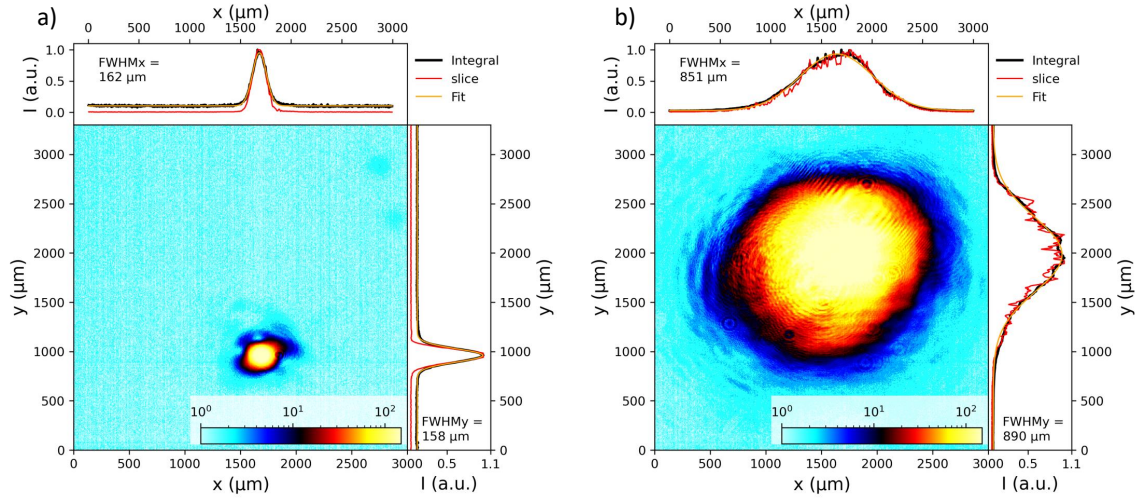


FIGURE 3.2: **Beamprofile for frontside excitation for pump and probe** a) probe profile with full width half maximum (fwhm) area of $162 \mu\text{m} \times 158 \mu\text{m}$; b) pump profile with fwhm area of $851 \mu\text{m} \times 890 \mu\text{m}$. These images were recorded using a commercial CCD-camera (Thorlabs DCC 1545M) at the sample position with a pixel size of $5.2 \mu\text{m}$.

For the backside excitation, the profile for the probe stays the same. The profile for the pump has a size of $841 \mu\text{m} \times 948 \mu\text{m}$. Using a top hat approximation which assumes that all the energy is stored in an elliptical $1/e$ footprint, the fluence is calculated as follows::

$$F = \frac{E}{1.44 \cdot A} = \frac{P}{1.44 \cdot \pi x_{\text{fwhm}} y_{\text{fwhm}} R'}$$

where R is the repetition rate of the laser system. The repetition rate for the probe is 1kHz, for the pump it's 500Hz. The resulting conversion factor C between power P in mW and incident fluence F in mJ/cm^2 , where $F = C P$, are listed in table 3.1

Setup	Pulse	Conversion
Frontside	Pump	0.23
Frontside	Probe	3.45
Backside	Pump	0.22

TABLE 3.1: **Conversion factor** between power in mW and fluence in mJ/cm^2

A relatively large pump laser spot size is chosen to match the excitation conditions at the Plasma x-Ray source (PXS) experiments, which are not discussed here in detail.

3.1.2 Characterization of the electro-magnet

To characterize the magnet, the magnetic field between the pole shoes is measured with a Hall Sensor. The distance between the pole shoes is 6mm. Measuring the magnetic field inside the magnet is essential since only the current through the magnet can be controlled in the actual experiment. If one can convert this current into the magnetic field, the behavior of the sample can be measured in dependence on the magnetic field.

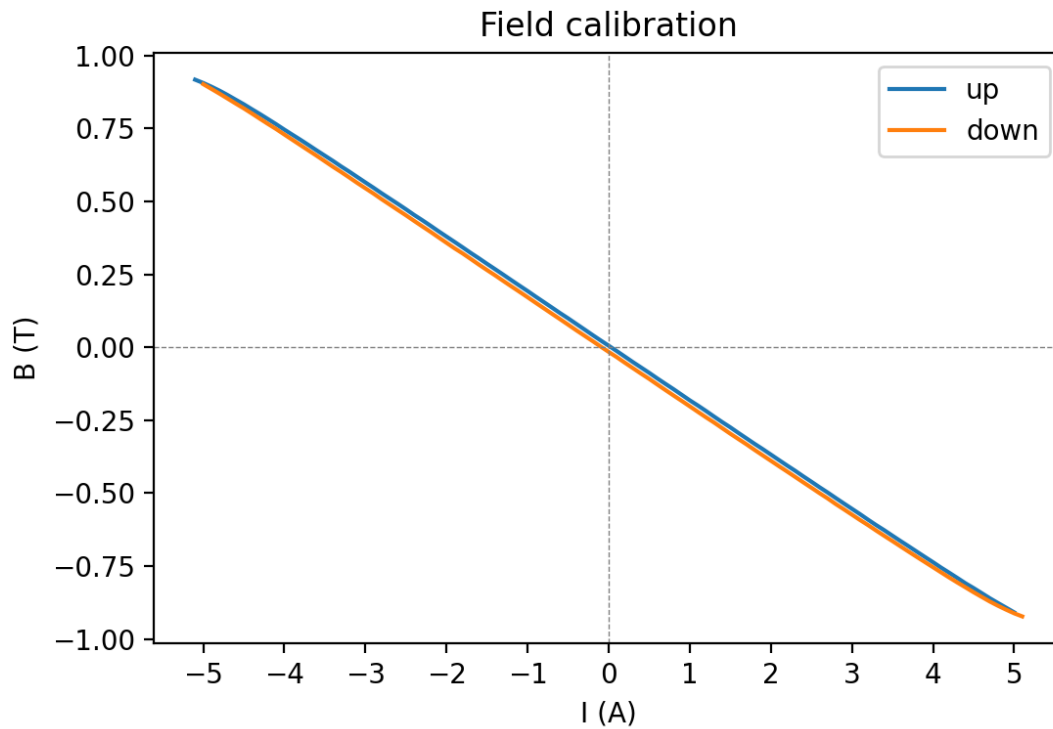


FIGURE 3.3: **Current dependence of the external B-Field** supplied by the commercial magnet GMW 3470. The magnet features custom-made pole-shoes with a facet of 20mm and holes that allow for optical access to the beams from both sides. Up means that the current is varied from -5 to 5A, and down means it is varied from 5 to -5A. The maximum field for the 6mm gap is approximately 900mT. The field is measured using a commercial Hall sensor (MAGSYS HGM09) at the sample position.

3.1.3 Samples

The samples used in the experiments vary in their thickness. Both thin film Nickel samples have been fabricated at the Max-Born institute in the group of Stefan Eisebitt. The 20nm thin film was created by magnetron-sputtering, similar to the samples in the paper by Borchert, and the 200nm thick film has been grown by thermal evaporation. The structure of both samples are the same, on a glass (SiO_2) substrate, 3nm thin films of tantalum and platinum are added, then a layer of Nickel of either 20 or 200nm follows. Moreover, as capping, a 2nm layer of platinum is deposited. In figure 3.4, the simulated absorption profiles under different conditions are shown. The calculation is based on the method by Koji Ohta, and Hatsuo Ishida [19]. The numerical implementation was developed by Loic Le Guyader [20].

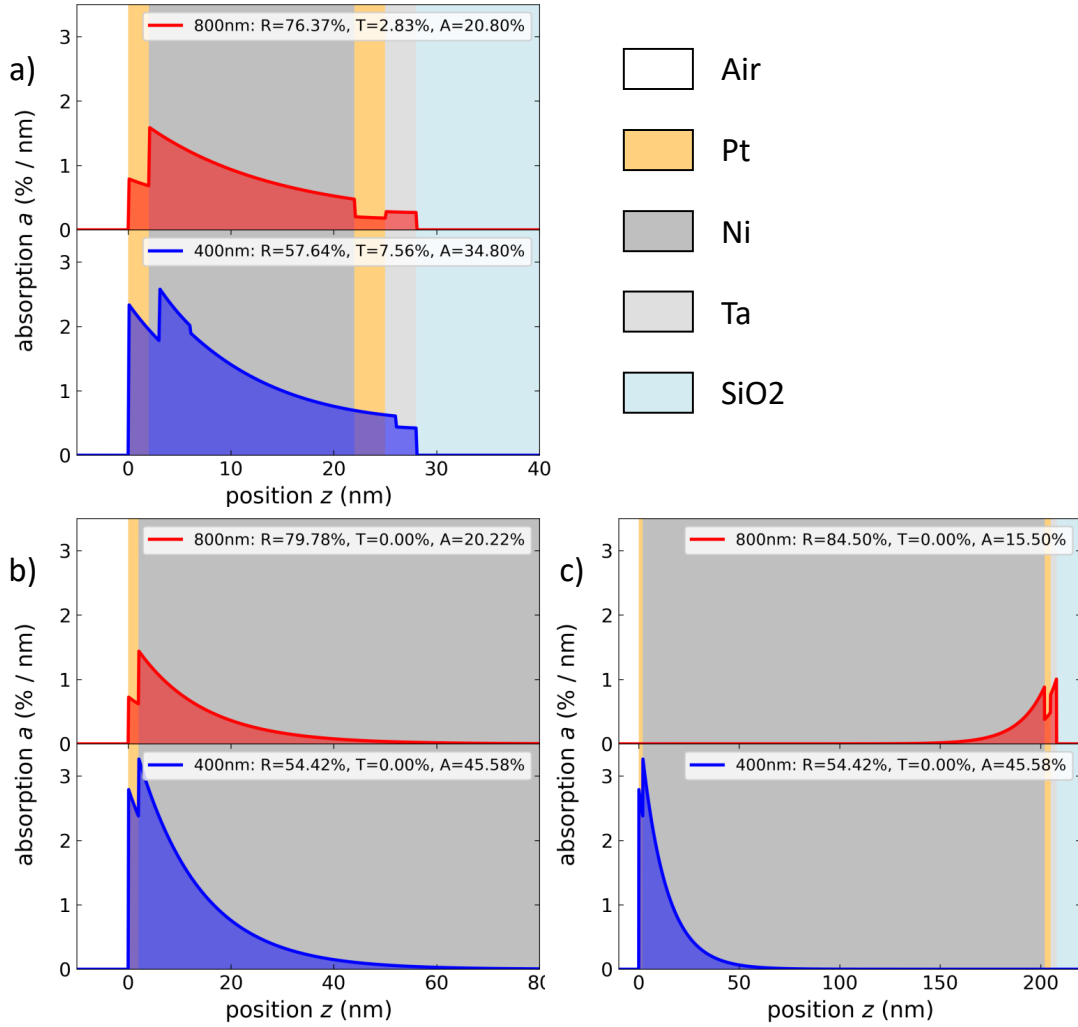


FIGURE 3.4: **Absorption profile of the samples:** a) 20nm Nickel layer front side excitation; b) 200nm Nickel layer front side excitation; c) 200nm Nickel layer backside excitation. The optical penetration depth is only 25nm, as it is common for a metallic specimen. The 20nm thin Ni film is thus excited relatively homogeneously, whereas the absorption is very inhomogeneous for the case of the 200nm film. For the 200 nm thin film, the MOKE signal probes only the near-surface region, whereas it probes the magnetization of the entire sample for the 20 nm film.

The absorption profile is important since the measured signal of the MOKE setup depends on the penetration profile. As an example, consider the magnetization of the sample. The magnetization M depends on depth (z) and time (t). The measured signal only depends on time. Let $A(z)$ be the absorption profile. Then the measured magnetization \mathcal{M} is given by:

$$\mathcal{M}(t) = \int A(z) M(z, t) dz. \quad (3.1)$$

For both samples, a hysteresis curve is measured. This is achieved by changing the magnetic field and measuring the MOKE voltage signal. The hysteresis curve for 20 and 200nm are shown in figure 3.5.

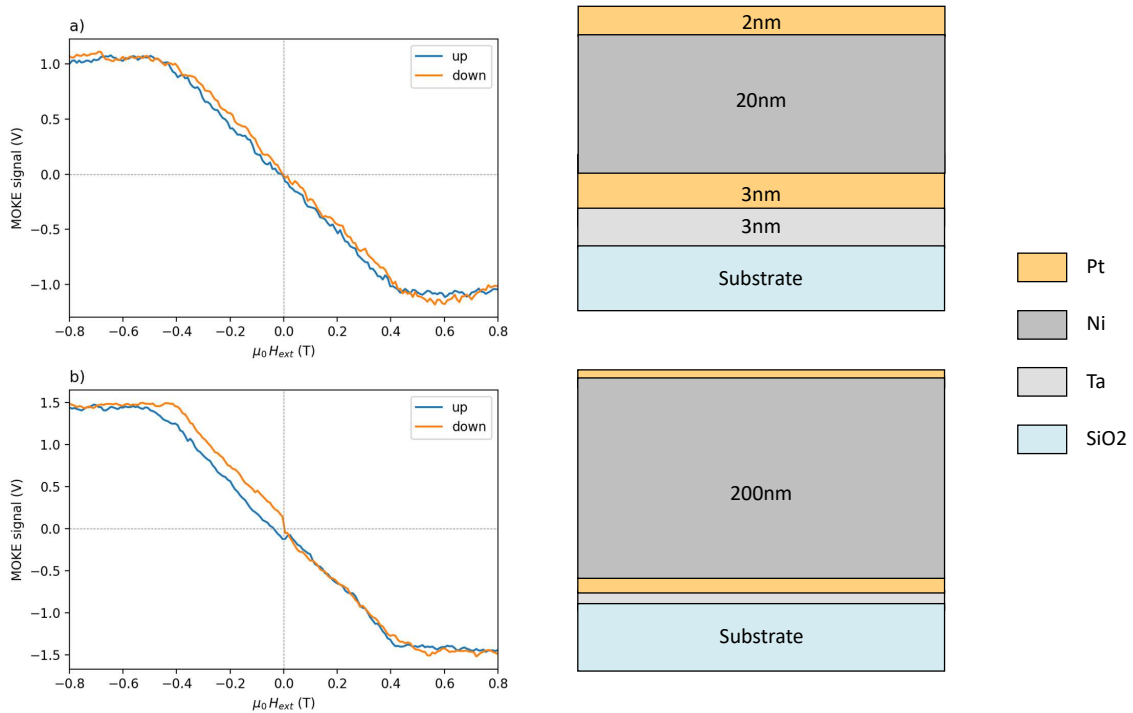


FIGURE 3.5: **Static hysteresis:** a) for the 20nm sample; b) for the 200nm sample; saturation is reached for both samples at $B \geq 0.5$ T. The level of saturation is higher for the 200nm sample. On the right side, the structure of the samples is depicted. Later measurements showed, that for the 200nm sample the gap between up and down does not depend on the direction of the external field.

The level of saturation is the difference between the highest and lowest MOKE signal is meant. This is important since the relative magnetization change can then be derived from the MOKE signal, as discussed previously.

3.1.4 Data analysis procedure

In the Wollaston prism, the light is separated into p- and s-polarized components. The relative difference between both polarization contributions is measured using a balanced photodiode (Thorlabs PDB210A). Since the difference between p- and s- polarized components is proportional to the magnetization, due to the MOKE-effect, one can obtain information about the magnetization dynamics. A detailed discussion can be found in [12] (p. 25ff). In the time-resolved measurements, the change in amplitude between the s- and p-polarized contributions of the reflected probe beam is recorded as a function of the pump-probe delay for positive and negative external magnetic fields. In other words, the difference signal of the balanced photodiode is measured. The resulting data for a 200nm Ni film is depicted in figure 3.6.

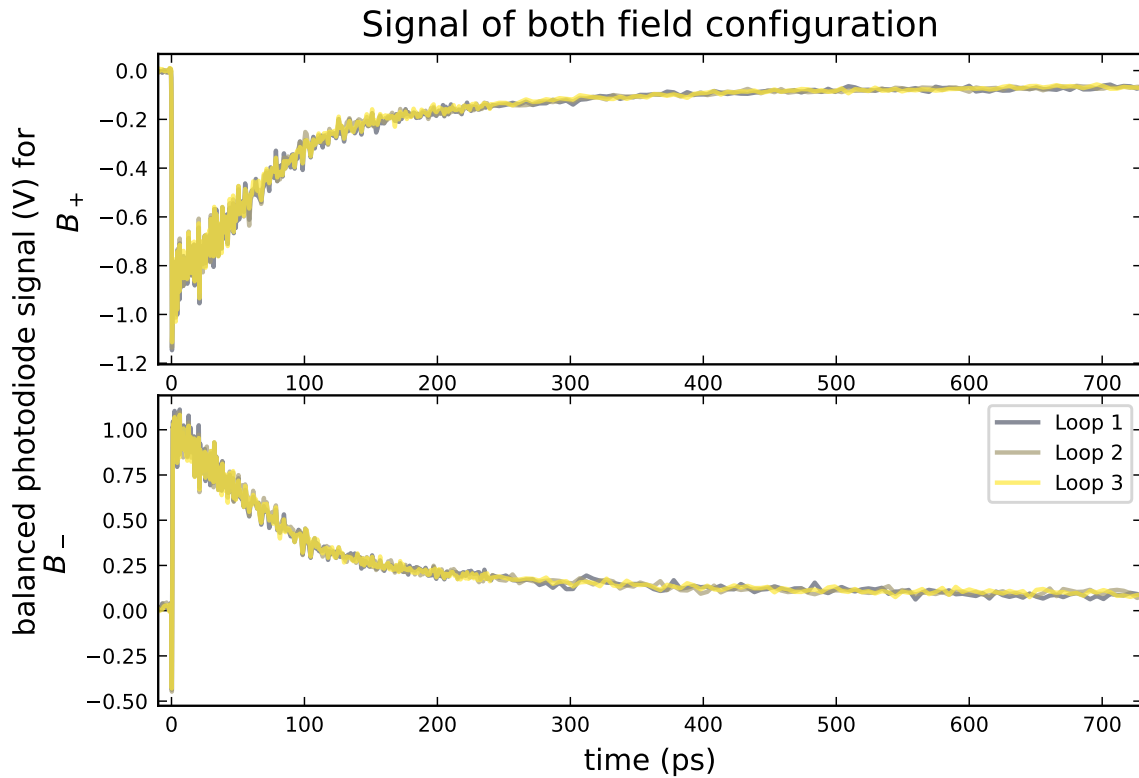


FIGURE 3.6: **Raw data of a trMOKE measurement** on for a directly excited 200nm Ni sample at an incident fluence of 26.4 mJ/cm^2 and an external field of 640mT.

Now the signals for both field directions can either be added together or subtracted. By adding them together, one obtains the polarization change that occurs independently of the orientation of the magnetization. When the signals for B_+ and B_- are subtracted from each other, one obtains the B-field dependent MOKE signal that is proportional to the out-of-plane magnetization. Figure 3.7 depicts the results of both operations. It shows that, for the given sample, we observe a relatively small non-magnetic Kerr-effect and a contribution that depends on the magnetization direction.

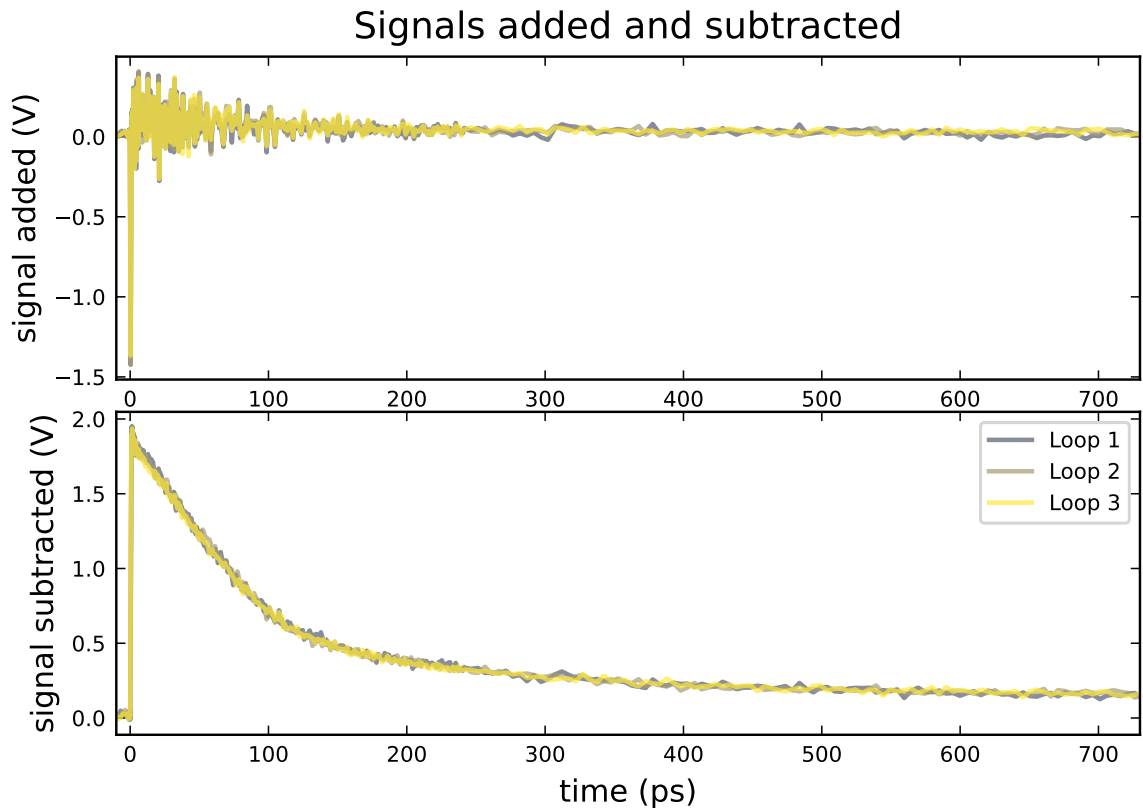


FIGURE 3.7: **Raw data added and subtracted:** The added signals shows the laser-induced polarization rotation that is independent of the external field. The bottom panel depicts the MOKE signal that depends on the sign of the out-of-plane magnetization.

The subtracted signal could either be used to describe the proportional magnetization or one can convert this into the relative magnetization. As one can see in figure 3.5 for the 200nm sample, the amplitude of the static hysteresis loop of the MOKE signal without laser-excitation is approximately 1.5V. Therefore, the resulting relative magnetization change can be calculated as follows:

$$M/M_{sat} = \frac{S}{2 \cdot 1.5V} + 1, \quad (3.2)$$

where S is the time-dependent MOKE signal in Volts. The result of this normalization process is shown in figure 3.8.

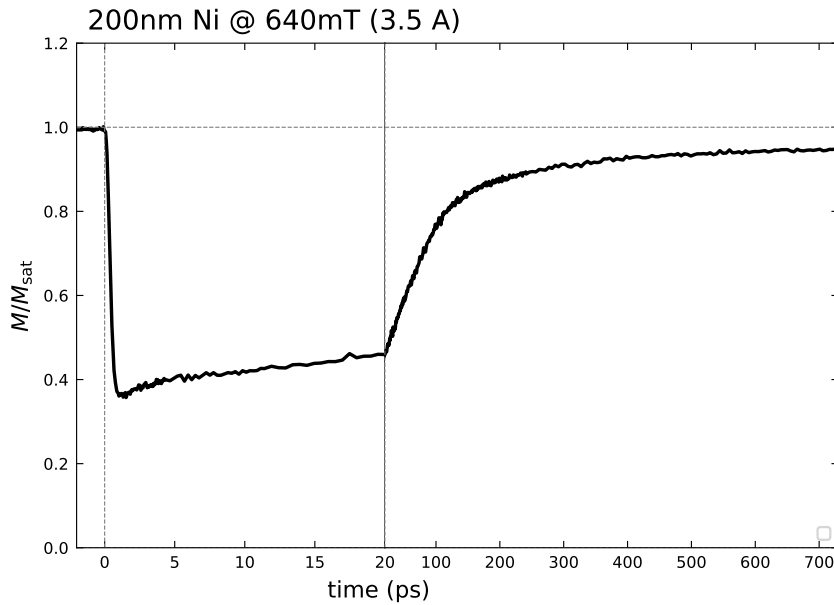


FIGURE 3.8: **Relative time-dependent magnetization averaged magnetization change for a 200nm Ni sample.** The x-axis is split at 20ps such that the fast demagnetization, and slow remagnetization are visible.

3.2 Front side excitation of the 20nm sample

In the following, the measurements for front side excitation of the 20nm sample are shown. The fluence dependence of the magnetization response are presented. The 20nm Nickel sample was measured at 180mT and 640mT, in order to identify a potential precession and a demagnetization behaviour.

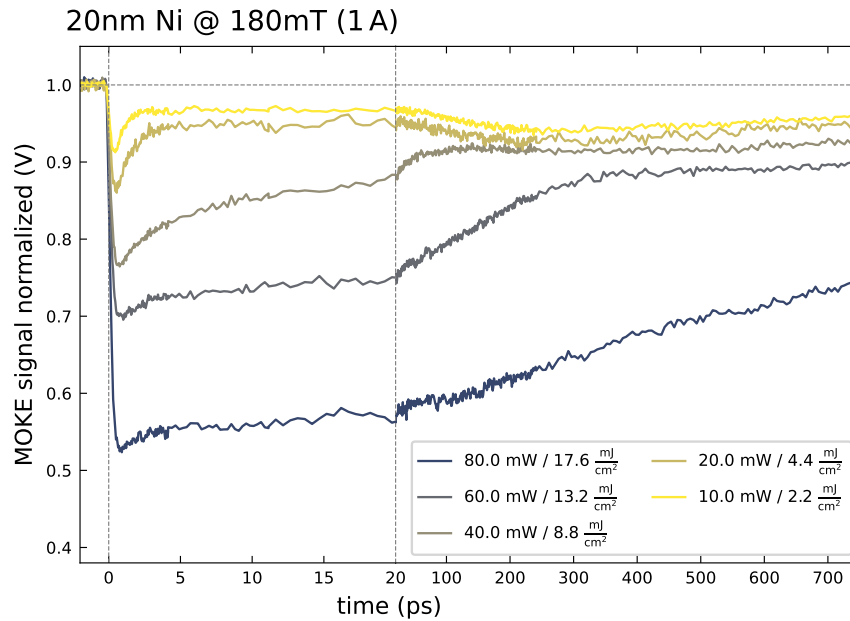


FIGURE 3.9: **Excitation fluence series for 20nm at $B = 180\text{mT}$** : While for low fluence remagnetization occurs on the picosecond timescale, the remagnetization for high fluences is 3 orders of magnitude slower. For low fluences, after remagnetizing, the magnetization goes down until 200ps and then increases again. This might be due to magnetization precession.

The remagnetization is different for different fluences. While for small fluences the remagnetization occurs on the picosecond timescale, the remagnetization for high fluence is much slower. In figure 3.10 the dynamics for a higher external field is shown.

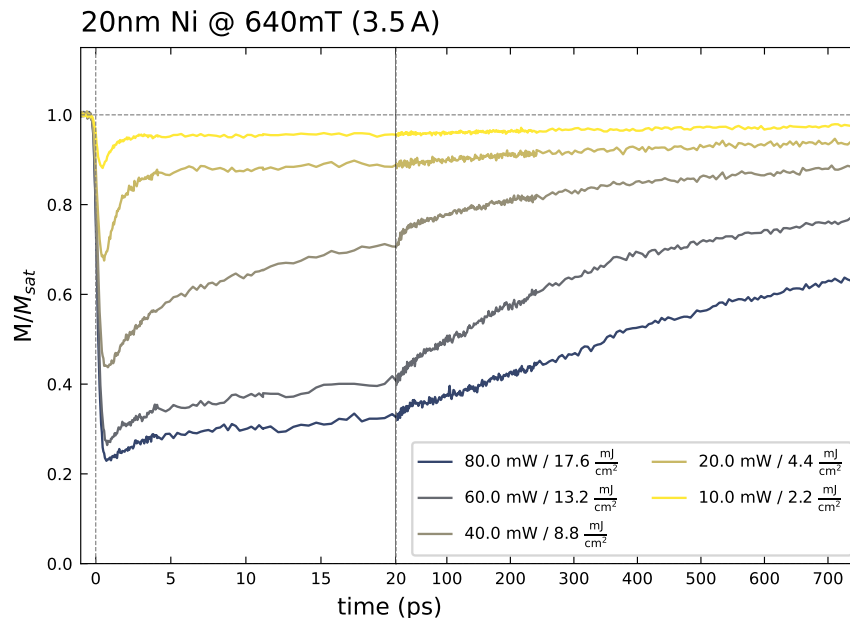


FIGURE 3.10: **Excitation fluence series for 20nm at $B = 640\text{mT}$** : No precession can be seen. Just as for the smaller field, the 2 types of remagnetization can be seen

One can see that the timescale on which the remagnetization occurs depends strongly on the incident fluence.

3.3 Front side excitation of the 200nm sample

In the following, the measurements for front side excitation of the 200nm sample are shown. The fluence dependence of the magnetization response and the dependence of the external field is presented.

3.3.1 Excitation fluence series for 200nm Nickel

The fluence series for the 200nm Nickel sample was measured at 180mT and 640mT. Since an external field of 180mT is below the saturation value, the y-axis shows a normalized MOKE signal in arbitrary units and not the relative magnetization change.

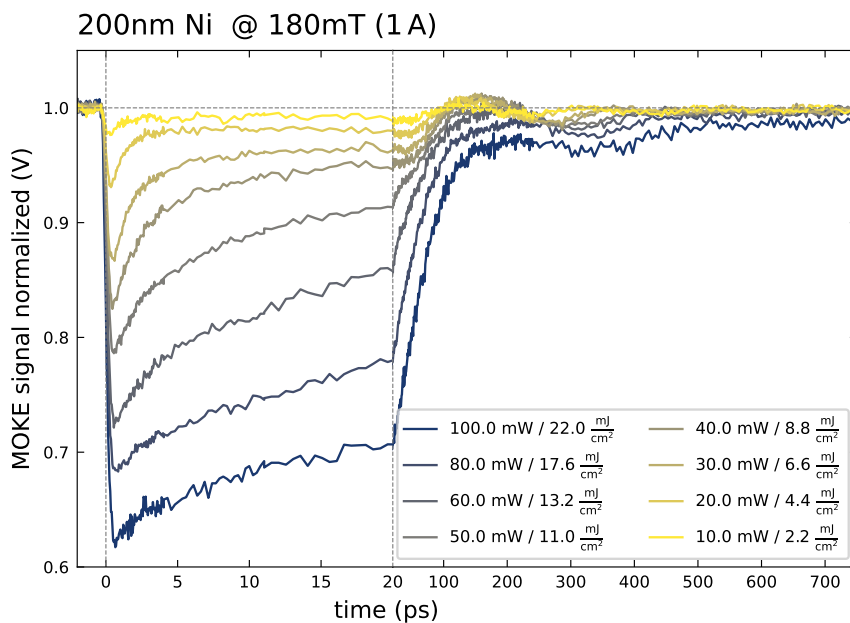


FIGURE 3.11: **Excitation fluence series for 200nm at B = 180mT:** Precession can be clearly seen. The precession frequency decreases for higher fluence. The higher the fluence, the higher the demagnetization.

In comparison, the measurements at a higher magnetic field, shows no precession at all. Both measurement show 2 different types of remagnetization. For B=640mT they are more distinct.

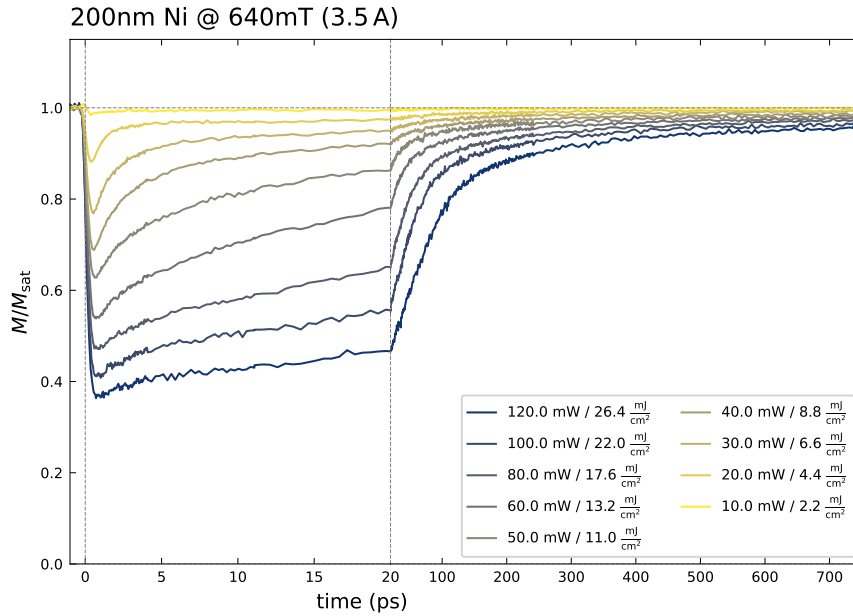


FIGURE 3.12: **Excitation fluence series for 200nm at B = 640mT:** No precession can be seen. The demagnetization level increases for higher fluence

For small fluences, the remagnetization is very fast. It occurs within 5ps. For higher fluences, the remagnetization is slower and occurs on the order of 100ps.

3.3.2 B-field series for 200nm Nickel

The B-field series for the 200nm Nickel sample was measured at a fluence of $F=3.5 \frac{\text{mJ}}{\text{cm}^2}$. In figure 3.13 the magnetization response for different external fields is shown.

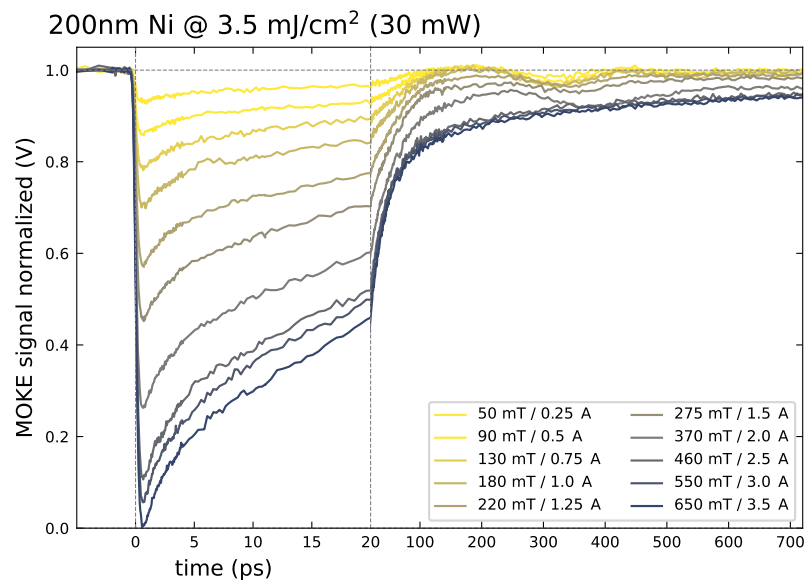


FIGURE 3.13: **B-field series for 200nm:** In this measurement one can clearly see the precession of the magnetization. It shows, that the precession is more distinct for a smaller/intermediate external field, and that the frequency decreases for higher fields.

3.4 Backside excitation of the 200nm sample

The other type of demagnetization can be observed when the pump and probe come from different sides. Like in the previous section, a systematic variation in the dependence of the magnetic field and fluency was investigated. As seen in figure 3.4, for the 20nm sample, the pump is absorbed homogeneously in the entire sample. Therefore, only the 200nm thick Nickel sample is investigated by backside pumping and front side probing geometry.

3.4.1 B-field series for 200nm Nickel

The demagnetization was measured at a fluence of $F = 24.2 \frac{\text{mJ}}{\text{cm}^2}$. The behaviour of the demagnetization is very different compared to the front side measurement.

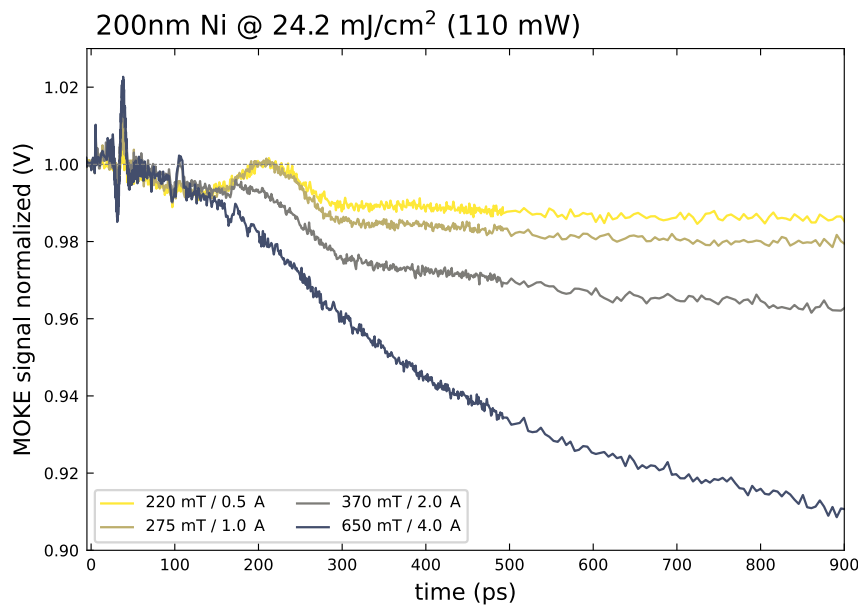


FIGURE 3.14: **B-field series for 200nm at $F = 24.2 \frac{\text{mJ}}{\text{cm}^2}$** : Precession can be clearly seen. For higher magnetic fields, the precession vanishes. For the timescale up to 200ps tripolar pulses can be seen, which might occur because of strain pulses in the sample.

3.4.2 Excitation fluence series for 200nm Nickel

The Excitation fluence series was measured at saturation, the magnetic field was at $B = 650\text{mT}$. The measurement shows an interesting feature. A tripolar-signal occurs periodically every 69ps.

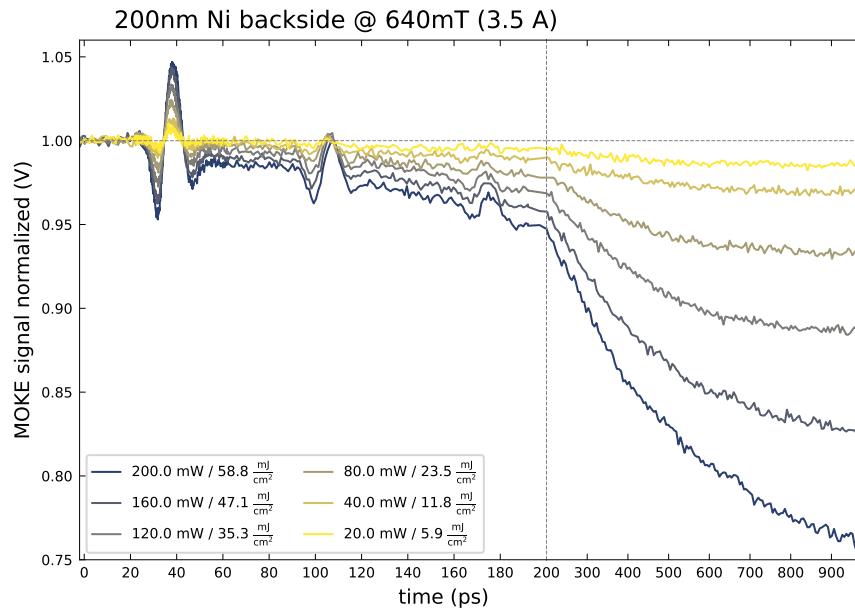


FIGURE 3.15: **Excitation fluence series for 200nm at $B = 650\text{mT}$** : Interesting tripolar features occur periodically with a distance of 69ps.

The tripolar feature seems to be a strain pulse propagating through the sample. One strong evidence for this is that the time difference of 69ps and a sound velocity in Nickel of 6 nm/ps yield 207nm, which is approximately the thickness of the sample. In the next chapter, all the presented measurements are analyzed in more detail.

Chapter 4

Discussion of the results

In this chapter, the experimental results presented in chapter 3 are analyzed and related to the theoretical models presented in chapter 2. First, the demagnetization is discussed using the python modeling library `udkm1Dsim`, which was recently upgraded to include magnetization effects. "The `udkm1Dsim` toolbox is a collection of Python classes and routines to simulate the thermal, structural, and magnetic dynamics after laser excitation" [21]. The toolbox helps to understand the magnetization response within the heterostructure using the m3TM and the 3TM for ultrafast demagnetization. The two different models are compared to the experimental observation in the MOKE measurement. In order to calibrate the structural response and the film thicknesses, the simulation of the strain response is compared to the results obtained at the Ultrafast X-ray diffraction setup in the UDKM-group. In the second part of this chapter, the dependence of the external field on the precession frequency is analyzed. In the end, a model to describe the tripolar pulse form of the MOKE signal in the backside measurements is developed.

4.1 Magnetization dynamics

The most prominent feature in the presented data is the ultrafast demagnetization after laser excitation and the subsequent remagnetization. The different excitation geometries, front side and backside pumping, are studied as two different phenomena. Since the coupling of electrons and phonons in Nickel is relatively strong, electrons will heat up when the material is excited but transfer their energy rapidly to the phonons. Therefore, if electrons are heated on one side of a 200nm sample, on the other side, their temperature increases more gradually. That is the reason why the front side and backside dynamics are so different. The models for the magnetization dynamics discussed in chapter 2 only work on concise time scales or for situations where spatial diffusion effects can be neglected. That is due to the reason that here a local system is described. The evolution only depends on time, and effects such as heat transport are neglected. In a more realistic scenario, one must describe how the temperature of electrons and phonons also depends on the position. To do this, the `udkm1Dsim` toolbox by Daniel Schick [21], that solves the set of differential equations 2.4-2.6 or for the m3TM the equations 2.10-2.12 is used. The simulated magnetization response is weighted according to the probe penetration profile described in section 3.1.3 in order to obtain a quantity that is comparable with the MOKE measurements. Using this toolbox, it is possible to compare the results of the 3TM and the m3TM for the 20nm thin Nickel film qualitatively. For the modeling, the parameters from table 4.1 are used.

Element	Nickel	Platinum	Tantalum	Silicon dioxide
heat capacity lattice (J/kgK)	442.20	133	140	719
Sommerfeld constant (J/kgK ²)	0.112	0.035	0.1809	none
thermal conductivity electrons	81.4	66	52	0
phonons (W/mK)	9.6	5	5	1.32
spin-lattice coupling (W/m ³ K)	13.5e15	none	none	none
electron-spin coupling (W/m ³ K)	270e15	none	none	none
electron-lattice coupling (W/m ³ K)	360e15	375e15	100e15	none
linear thermal expansion coefficient lattice (1/K)	11.8e-6	8.9e-6	6.3e-6	none
linear thermal expansion coefficient electrons (1/K)	3.88e-9	8.46e-10	2.11e-9	none
sound velocity (nm/ps)	6 [22]	4.242	4.15	5.832 [23]
refractive index for 800nm & 400nm	2.218+4.8925i 1.7163+2.5925i [24]	0.57617+8.067i 1.0433+3.0855i [25]	0.99181+7.293i 1.3259+3.5442i [25]	1.45 [26]
density (g/cm ³)	8.908	21.45	16.678	2.65 [27]
Poisson correction factor	2.26	2.2	2.03	none
layer structure	amorphous	amorphous	amorphous	amorphous
R (ps ⁻¹)	17.2 [3]	none	none	none

TABLE 4.1: **List of the simulation parameters:** The parameters shown are used in the udkm1Dsim toolbox. Heat capacity and thermal conductivity for SiO₂ are from [28]. Electron-spin as well as spin-lattice coupling are chosen such that their relative magnitude compared to the electron-lattice coupling is the same as in [2]. All other not referenced parameters are taken from Pudell 2020 [7].

4.1.1 Demagnetization by direct excitation.

In this subsection, the different models are compared with the measurement. The dynamics are studied up to 20ps after the excitation. In this first picture, the demagnetization for 20nm Nickel is simulated using the udkm1Dsim toolbox. Figure 4.1 provides an overview of the Spatio-temporal evolution of the electron and phonon temperatures as well as the resulting magnetization for both models. The excitation power is chosen such that the demagnetization level for the two models are comparable.

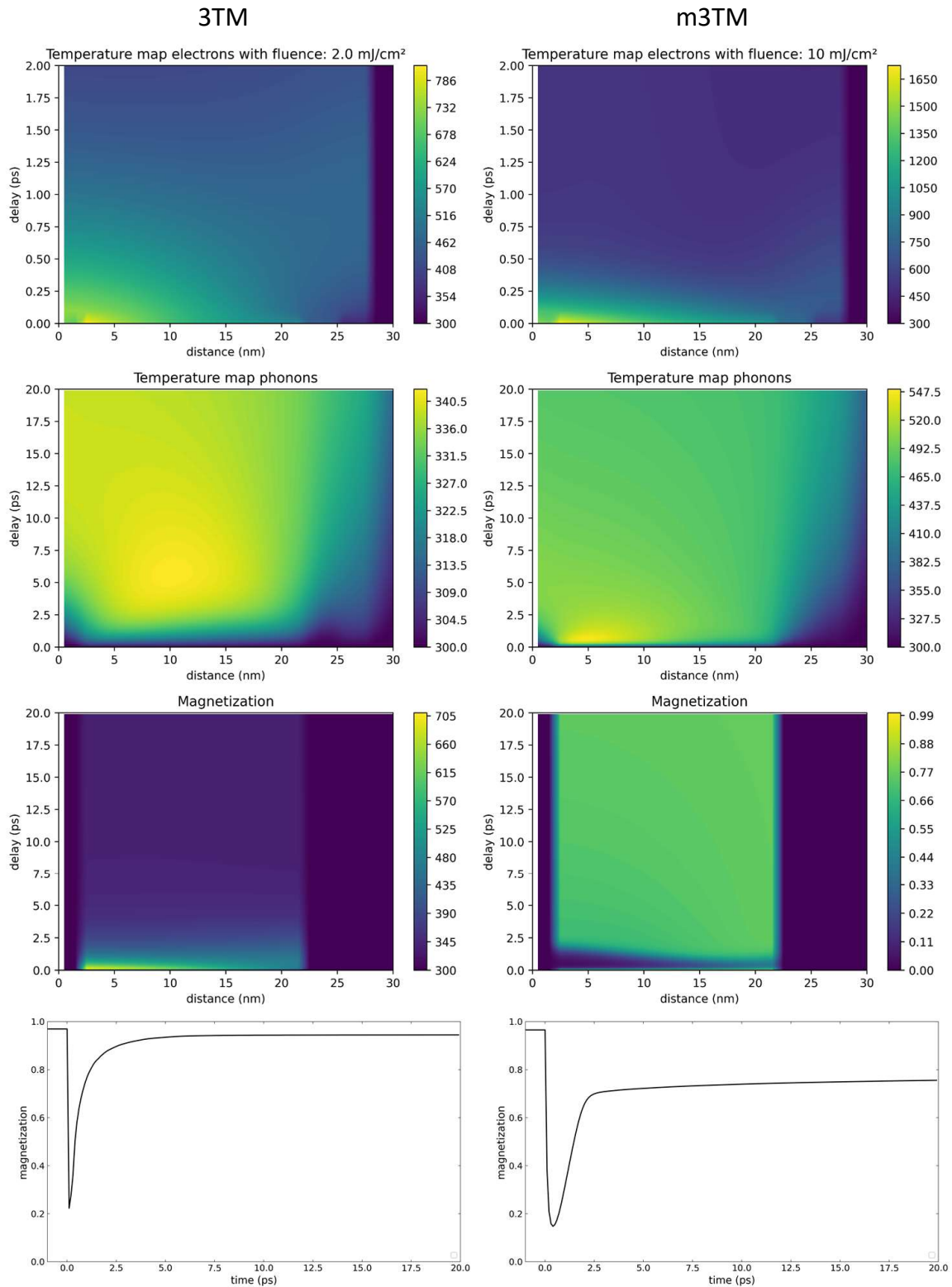


FIGURE 4.1: **Comparison of the two magnetization models for 20nm Nickel.** On the left side the spatial and time evolution for the 3TM is depicted. On the right side the evolution for the microscopic model is shown. On the bottom the resulting magnetization dynamics are depicted for both models.

In figure 4.2 the temporal evolution for different fluences are compared.

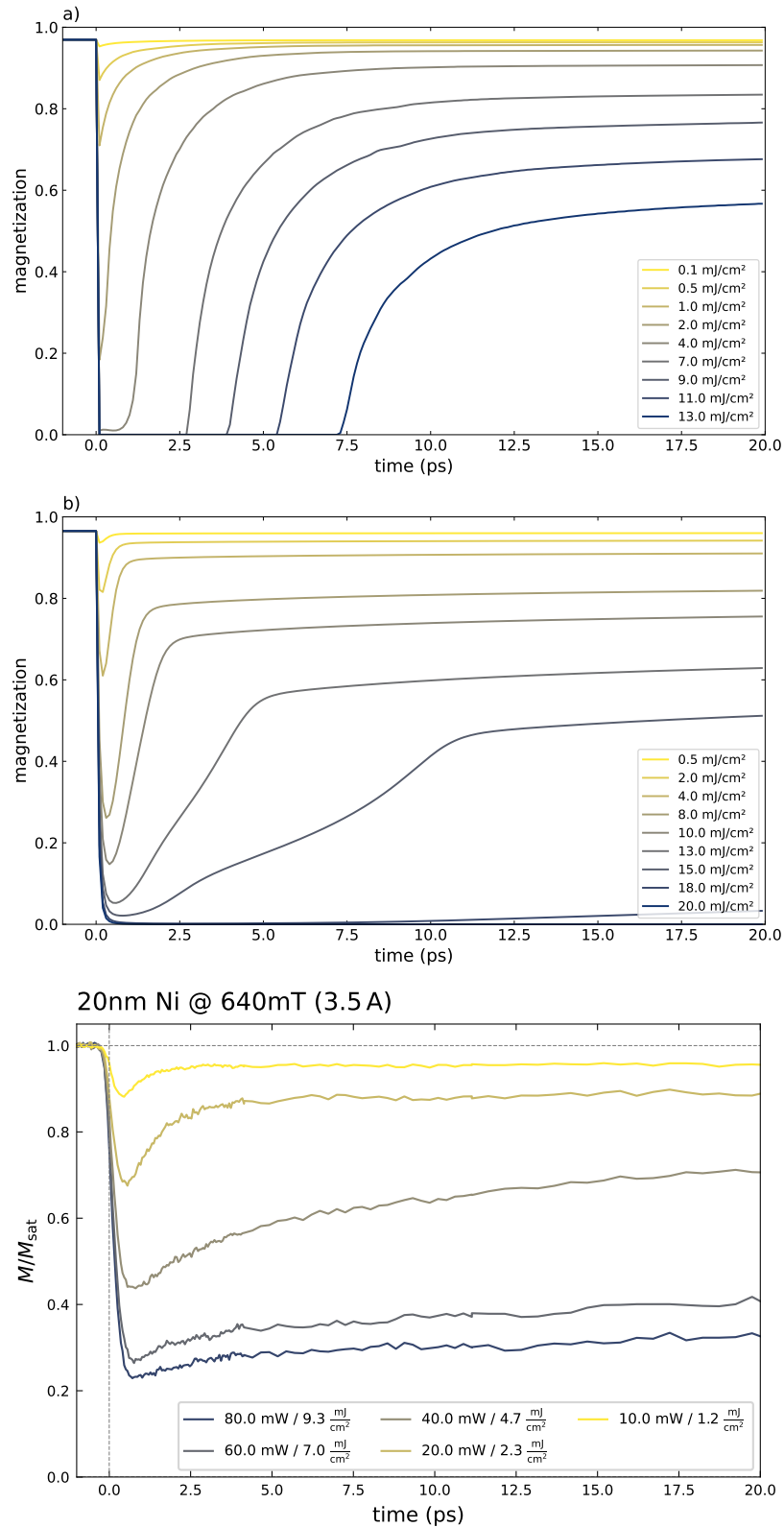


FIGURE 4.2: **Simulated magnetization response upon direct excitation for the 20nm Nickel sample.** a) this simulation uses the 3 temperature model; b) this simulation uses the microscopic temperature model. For comparison in the last panel the measured magnetization response is depicted.

Although the simulation does not match perfectly with the measurement, one can still

derive the qualitative features that arise in this numerical model. First, it seems like the microscopic temperature model matches better with the measurements. This can be seen particularly at the timescales of remagnetization. While the three temperature model only shows fast remagnetization, the m3TM shows two different types of remagnetization. A fast one occurs in the first picoseconds, and a slow remagnetization can be observed for higher fluences. One obvious difference between measurement and simulation is that while the real sample still has some magnetization left, the simulations show that the magnetization vanishes for high fluences. Similar experimental results, where some magnetization is still left, are reported in other experiments exploring the MOKE response in the high fluence regime. [29] [30], [13] [6] The origin of this saturation of the MOKE signal at high fluences has been debated [31] and potential contributions arise from a state filling effects in the transient electronic band structure that modify the MOKE response [32] or non-local effects in films of finite thickness, where the demagnetization is incomplete across the thin film [31]. This explanation is not suitable with the simulations done for the 20nm sample since for high fluence, the simulation shows complete demagnetization along the whole sample. Another plausible explanation for the difference between simulation and measurement might be domain effects. A small residual paramagnetic contribution to the MOKE signal might contribute furthermore.

Similar results are obtained from the simulation of the 200nm sample. In figure 4.3 the dynamics of the electron and phonon temperature, as well as the magnetization response for the 200nm sample, are depicted. As for the 20nm sample, the excitation fluence is chosen such that the demagnetization level for the two models is comparable.

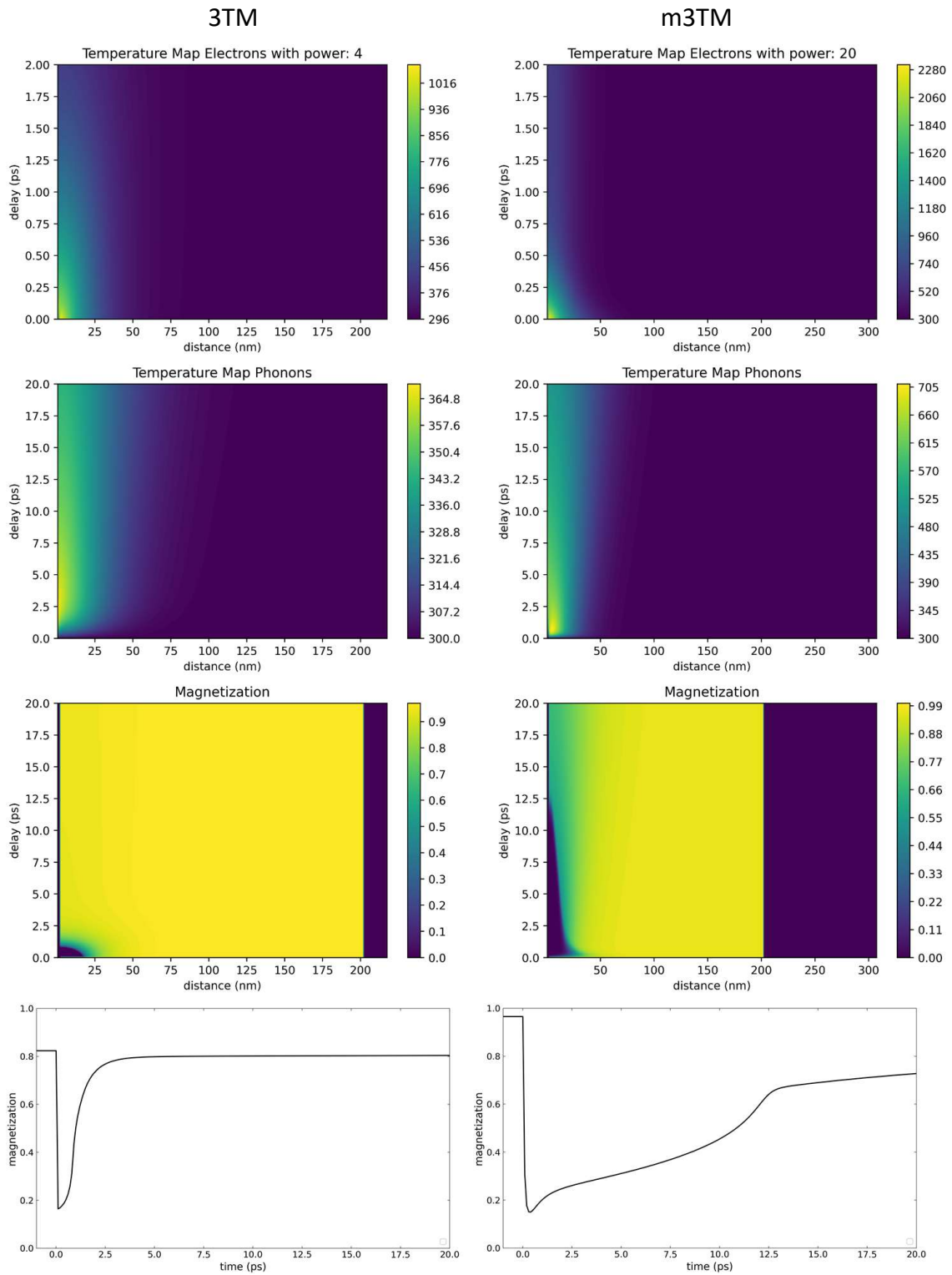


FIGURE 4.3: **Comparison of the two magnetization models for 200nm Nickel.** On the left side the spatial and time evolution for the 3TM is depicted. On the right side the evolution for the microscopic model is shown. On the bottom the resulting magnetization dynamics are depicted for both models.

In figure 4.4 the temporal evolution for different fluences are compared.

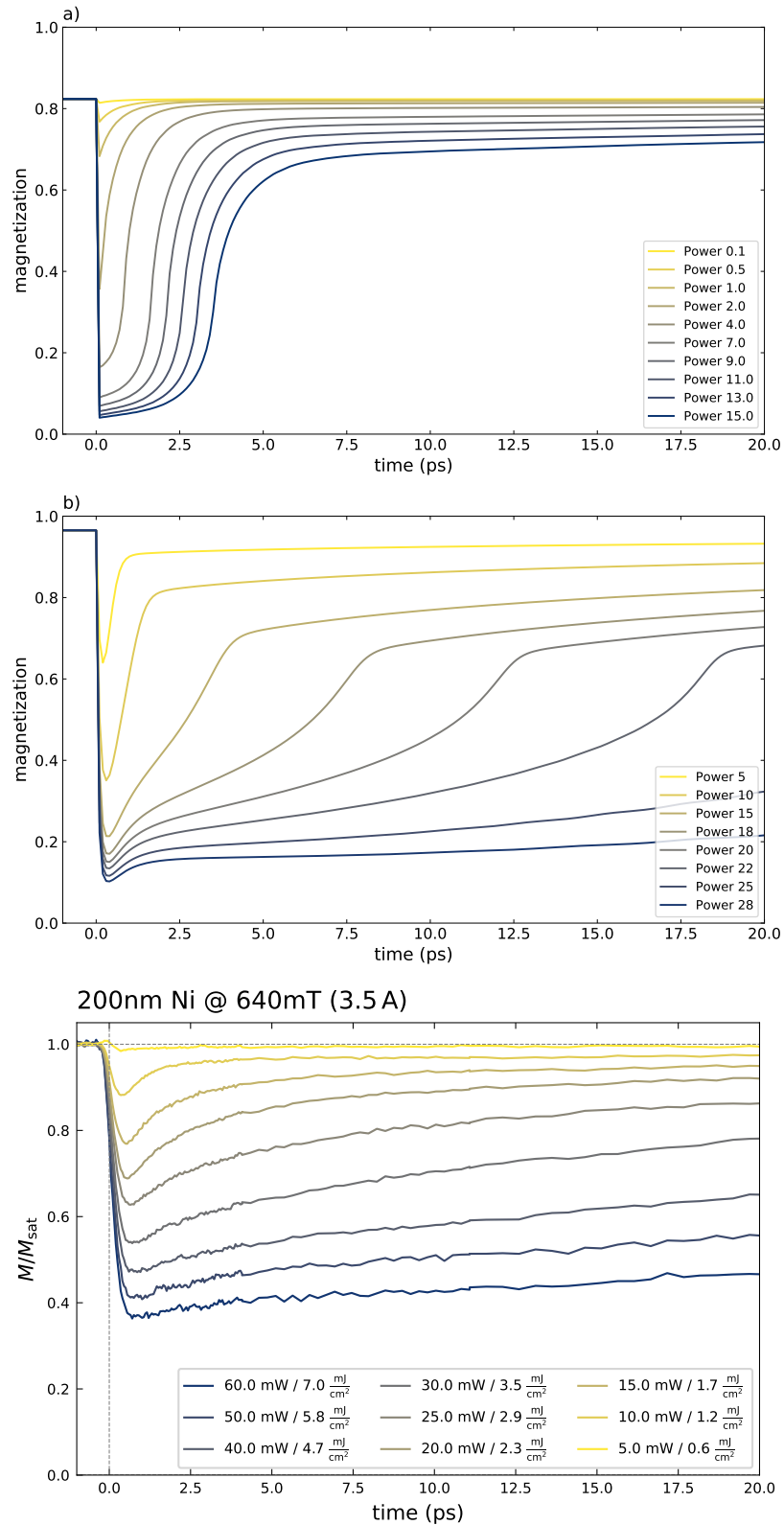


FIGURE 4.4: **Simulated magnetization response upon direct excitation for the 200nm Nickel sample.** a) this simulation uses the 3 temperature model; b) this simulation uses the microscopic temperature model. In the last panel the measured magnetization response is depicted.

Both simulations have in common that the interesting physics happens in the first 50nm

of the sample. One result is that the magnetization does not go down to zero because the sample does not demagnetize along its whole length. Also, the behavior of the electron and phonon sub-system are pretty similar. First, the electrons heat up very fast, then energy is transferred into the phonon and magnetization sub-system. While in both simulations, electrons and phonons reach equilibrium after 5 to 10ps, the magnetization dynamics are quite different. In the 3TM, the remagnetization is extremely fast and happens in 2.5ps, the microscopic model shows a more gradual remagnetization in order of 10ps.

4.1.2 Demagnetization by indirect excitation

For the simulation of the backside excitation using the m3TM, a workaround is used to ensure numerical stability in the very high excitation regime. One needs this since, for high fluences, the simulated magnetization drops below zero, which is a non-physical result. However, simulating the magnetization is still possible by splitting the 200nm Nickel layer into two layers. To circumvent the numerical artifacts that occur in the pumped sample region, the magnetic properties are only extended to the second half of the layer that is not directly excited. This assumption works well since the thermal conductivity of the magnetization in this model is zero, and the temperature of electrons and lattice does not depend on the magnetization. The assumed sample and its absorption profile are depicted in figure 4.5.

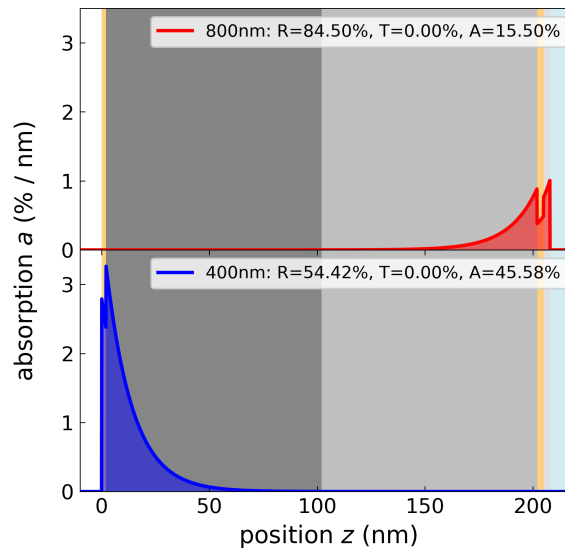


FIGURE 4.5: **Sample structure for m3TM simulation:** The light grey Nickel layer has no magnetic properties. The dark grey layer has the same properties as for the other simulations.

As seen in the figure above, it is reasonable to only consider the magnetization in the dark gray layer since the proportion of the blue light in the light gray layer is negligible. The resulting magnetization response is depicted in figure 4.6.

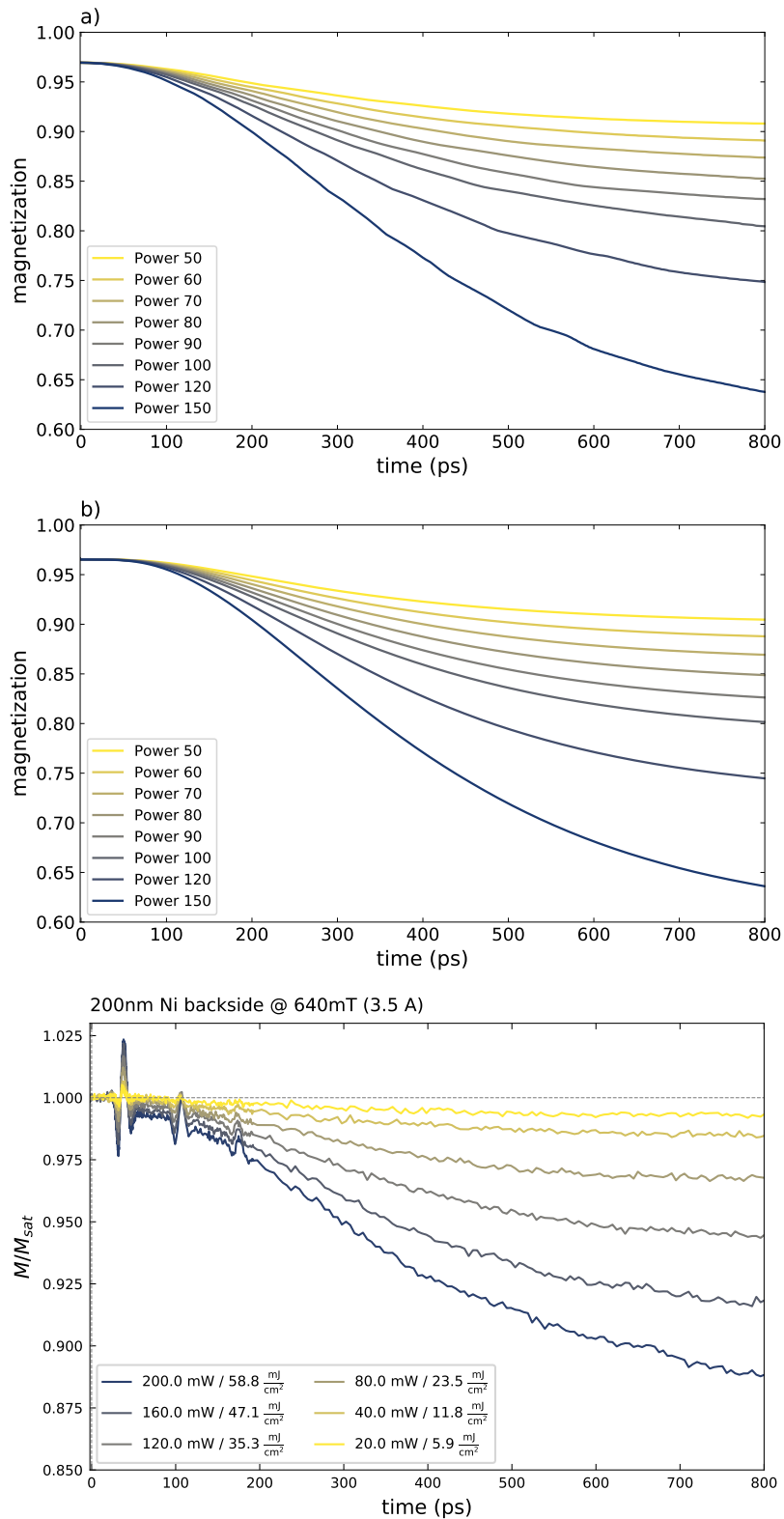


FIGURE 4.6: **Simulated magnetization response upon indirect excitation for the 200nm Nickel sample.** a) this simulation uses the 3 temperature model; b) this simulation uses the microscopic temperature model. In the last panel the measured magnetization response is depicted.

Both simulations yield nearly the same result and match well with the measurements. It

shows that both models capture the demagnetization by heat transport in thermal equilibrium. But not only does their behavior match, but also the input power is the same. This is quite different in the case of front side excitation, where the input power for comparable demagnetization results differs significantly.

4.2 Analysis of the magnetization precession

In the measurements shown in figure 3.13 and 3.14, precession can be seen. In figure 4.7 and 4.8 the precession is analyzed by fitting the the overall demagnetization dynamics with the red curve. On the bottom right, the difference between the fitted curve and the measured magnetization response is depicted. On the top right, the Fourier transform is shown.

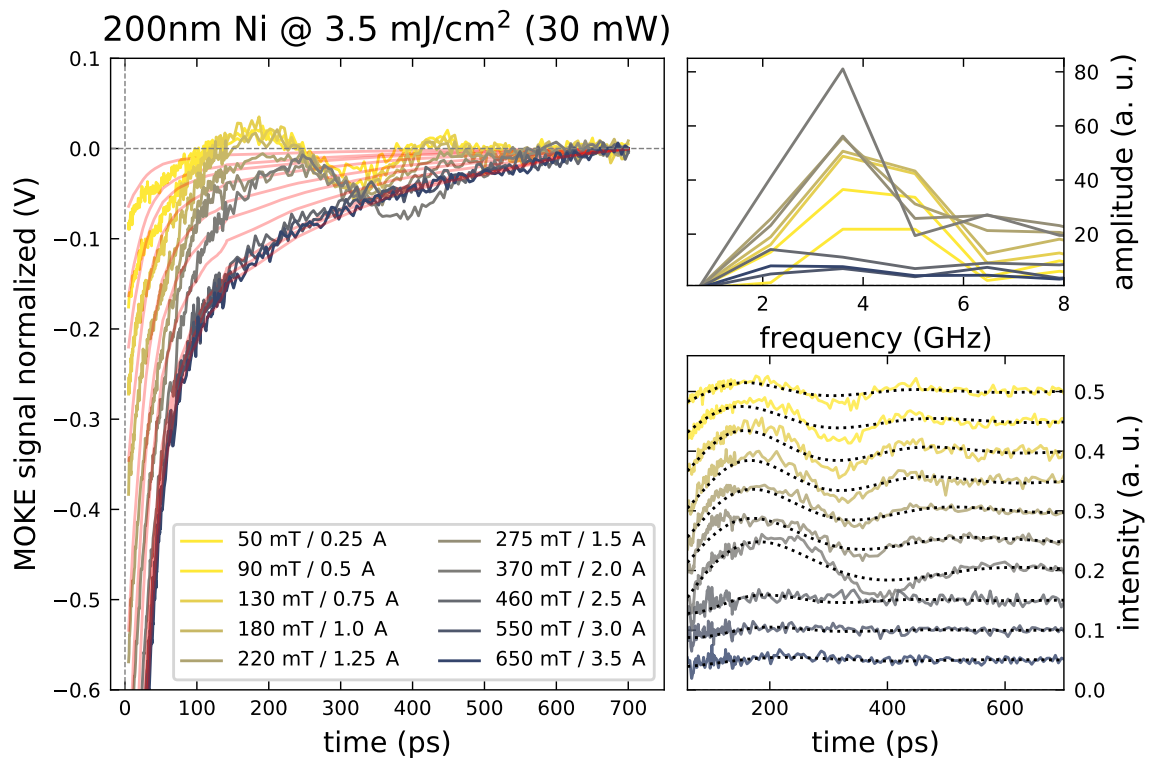


FIGURE 4.7: **Analysis of precession for 200nm Nickel front side pumping.** One can clearly see that by increasing the external field, that the precession frequency gets smaller. For a high external field the precession vanishes.

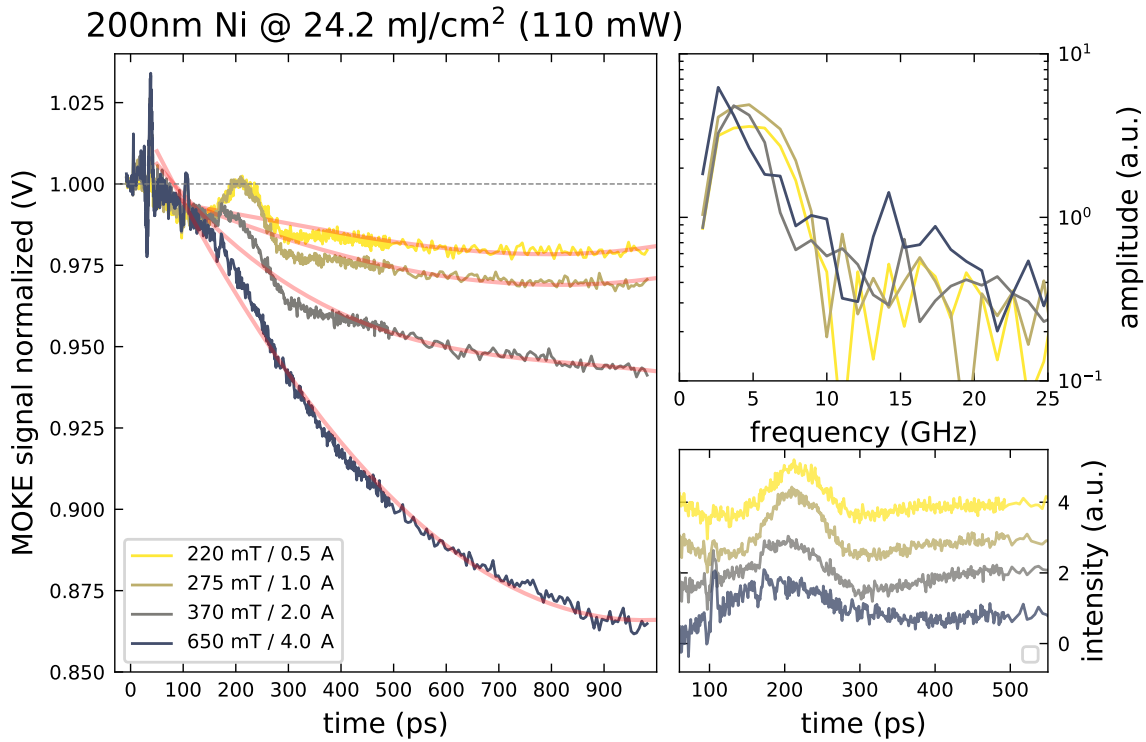


FIGURE 4.8: **Analysis of precession for 200nm Nickel backside pumping.** The precession frequency increases for smaller external fields. For a small fields the precession is more distinct.

That is a contradiction to equation 2.18 and the depicted behaviour in figure 2.5. One would expect that by increasing the external field, the effective field increases, and so does the precession frequency. The reason for this seemingly paradoxical behavior is the effective field. In the model used to create figure 2.5, the effective field was simply the sum of the anisotropy field and the external field. Actually, the effective field is more complex and can be written as [33], p. 27:

$$\vec{H}_{eff}(z, t) = \left(H_z - \underbrace{M_s m_z(z, t)}_{H_d} \right) \vec{e}_z + \underbrace{\frac{2K_x(z, t)}{\mu_0 M_s} m_x(z, t) \vec{e}_x}_{H_u} + \underbrace{2b_1 \eta_{zz}(z, t) m_z(z, t) \vec{e}_z}_{H_{me}} \quad (4.1)$$

$$- \underbrace{\frac{2K_k}{\mu_0 M_l} c_{ijk} \left(m_i^2(z, t) + m_j^2(z, t) \right) \vec{e}_k}_{H_c} \quad (4.2)$$

where c_{ijk} is defined via the Levi Civita symbol as $\epsilon_{ijk} = c_{ijk} - c_{kji}$. H_d denotes the demagnetization field, H_u the uniaxial anisotropy field, H_{me} the magneto-elastic field, and H_c the cubic anisotropy field. K denotes the different anisotropy constants, η is the strain. Just by looking at the first term, our contradiction can be resolved. When the external field (pointing in z direction) is increased, the magnetization in z direction also increases until m_z is equal to one. That means that until saturation of m_z is reached, the demagnetization may dominate the signal. Therefore, although the external field is getting bigger, the effective field shrinks. Since the precession frequency is proportional to the effective field, the precession frequency decreases for higher external fields. If the external field is increased even more, such that the demagnetization term is in saturation, the effective field gets bigger and

so does the precession frequency. A similar behavior was demonstrated experimentally for thin films of a bismuth-substituted yttrium iron garnet [34].

4.3 Analysis of the strain response

The rapid energy deposition within the sample leads to the generation of strain pulses. In figure 4.9 data with a clearly visible tripolar feature is shown. The dynamics without strain are fitted with the red line, such that the pulses can be extracted. On the top right, they are shown. On the bottom right, the amplitude of each strain is depicted.

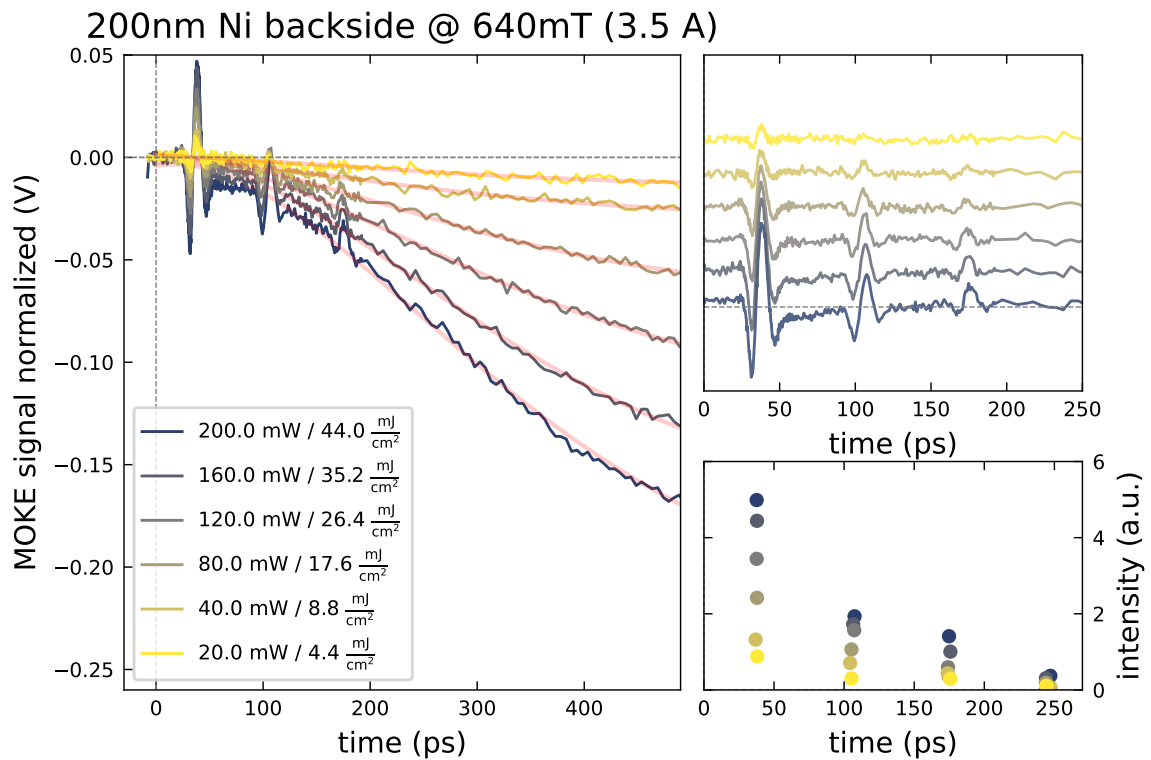


FIGURE 4.9: **Analysis of strain dynamics for 200nm Nickel backside pumping.** The amplitude of the strain pulses increases with higher fluence. The time between two pulses is approximately 69ps.

In this section, the shape of these features is discussed. Since strain pulses are bipolar, one might expect such a shape to occur in the figure 4.9. The difference can be explained by remembering equation 3.1. If one weighs the strain pulse in the sample, coming from the left, then getting reflected and propagating to the right, the time-dependent signal exhibits the tripolar shape that is depicted qualitatively in figure 4.6. This is in good agreement with our observed signatures that have also been seen by Kim et al. [22] and Thomson et al. [35].

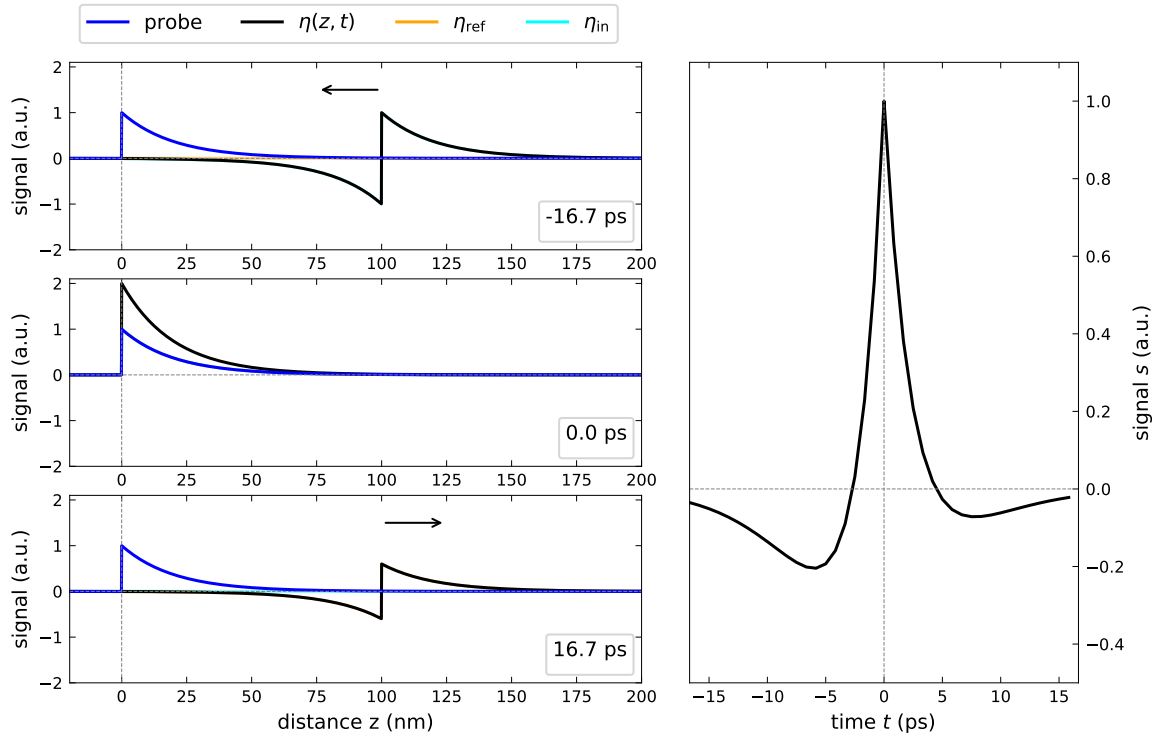


FIGURE 4.10: **Qualitative simulation of the shape of the strain pulse.** bipolar strain pulse, which moves to the left and gets reflected on an air-sample interface with a speculated reflectivity of 60 %. The remaining fraction of the strain wave is scattered diffusely. The strain is weighed with the blue curve, which indicates the probe profile. The resulting time-dependent signal is depicted on the right side.

In this qualitative model, a perfectly sharp and symmetrically bipolar strain pulse is assumed. Deviations of the observed signal from the modeled shape may arise due to different shapes of the strain pulse that may arise due to non-linear phonon-phonon interactions and damping effects of high-frequency phonon components [36] and finite heat diffusion during the strain generation [35] that are not the main focus of this work.

The periodical recurrence of the signal matches the expected round-trip time of strain pulses within the metal stack. Due to the significant acoustic impedance mismatch with the substrate, the strain-waves undergo multiple round-trips before their damping by partial transmission to the substrate leads to their disappearance. As mentioned before, the thickness of the sample and the sound velocity of Nickel yield a period duration of approximately 69ps. A confirmation for the validity yields the measurement done by Steffen Zeuschner and Maximilian Matterns in the PXS-lab for the 20nm sample. Here the time-dependent average strain is measured. This measurement can be directly compared with the simulations done for the 20nm sample. In figure 4.11a and 4.11b, the data and the simulation are shown.

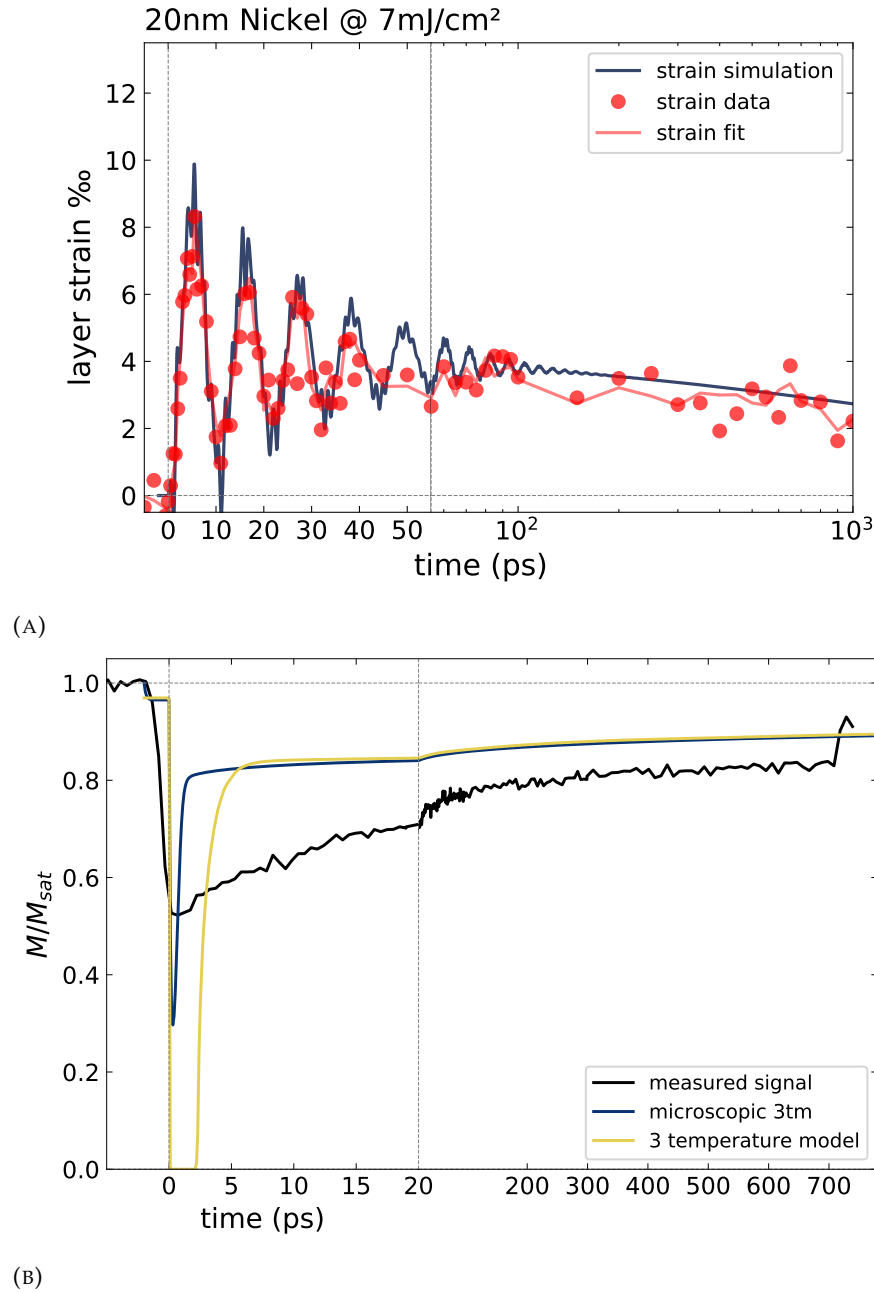


FIGURE 4.11: **Strain and magnetization dynamics for 20nm Nickel at $F = 7\text{mJ}/\text{cm}^2$.** (A) Simulation of the strain dynamics compared with measurements done in the PXS-laboratory. (B) Measurement of the magnetization compared to simulation using the two different models.

The strain simulation is similar compared with the data measured in the PXS-lab. For short-time scales, the oscillation in the strain pulses matches very well. The best agreement has been obtained by setting the thickness of the Nickel layer to 18nm. The damping of the strain oscillations occurs faster in the measurement as compared to the simulation. This may be due to surface roughness effects that would lead to a dephasing over time. The general trend of the thermal transport is captured by the udkm1Dsim simulation of the strain that uses the parameters listed in table 4.1.

The simulated magnetization response for the m3TM fits better than the 3TM to the measurement.

Chapter 5

Conclusion

5.1 Summary

The measurements done with the trMOKE setup yield good results and show that it is possible to measure trMOKE signals on Nickel with this setup. Three different experimental excitation conditions were measured. A 20nm thin film and a 200nm thick film both in direct excitation. And a 200nm thick film in indirect excitation. In all of these cases, the results in the saturation field and at half of the saturation field were compared to study the demagnetization and potential magnetization precessions.

For the 20 nm thin film in direct excitation, a subpicosecond demagnetization that recovers within 5ps in the low fluence regime is found. This can be attributed to the cooling of electrons to phonons. In the high-fluence regime, the demagnetization lasts for hundreds of picoseconds. Here the remagnetization seems to be limited by the cooling of phonons to the substrate.

For the 200 nm thick film in direct excitation, a similar subpicosecond demagnetization as for the 20nm thin-film is found. In the high fluence regime, the magnetization recovery in the probed fraction of the film is faster than the thin film results due to thermal transport effects within the inhomogeneously excited layer.

For the indirectly excited 200nm film, a slow demagnetization on a timescale of hundreds of picoseconds is observed due to the thermal transport of energy into the backside of the layer.

To rationalize the experimental results and test its capabilities, the newly relaunched python library `udkm1Dsim` [21] was used. The upgraded code includes magnetization modeling via a microscopic three-temperature model and a model for the penetration of the optical light within heterostructures based on a transfer matrix model. This extends the existing capabilities in modeling the strain response and the N-temperature models of the laser-excited samples of the previous Matlab library.

The modeled strain response for the 20nm film agrees with the experimental observations obtained by UXRD in the group, demonstrating the validity of the used thermo-physical parameters of the investigated films.

The magnetization response in the low fluence regime within the first five picoseconds is captured qualitatively by the 3TM and the m3TM. Only the m3TM can achieve a qualitative agreement of the demagnetization in the high fluence regime. However, numerical instabilities that lead to a negative magnetization have been encountered when modeling the high fluence response in the m3TM.

The observed magnetization precession was strongly damped and not as pronounced as in previous works by van Kampen et al. [37], or Kim et al. [22]. This is mainly due to the magnet setup in the polar MOKE geometry of the sample, where the field can only be applied along the out-of-plane direction of the sample. The demagnetization field reduces the

externally applied field, which leads to a relatively small effective field when the magnetization points at 45° to the sample surface. Upon increasing the external field, the magnetization points more out-of-plane, which reduces the precession amplitude. A variable field at oblique angles to the surface would be preferential for future precession studies with high-frequency spin waves.

The results obtained in this thesis represent a vital reference for the time-resolved MOKE experiments integrated at the ultrafast X-ray diffraction setup in the group. The extension of the MOKE setup now allows for both front-side and backside excitation of the samples, which is beneficial for all-optical studies in heterostructures due to the finite penetration depth of the light.

5.2 Outlook

In the future, the trMOKE setup will be developed further. In order to access the long-term magnetization dynamics, a 4ns stage and beam pointing stabilization will be implemented. Also, applying a B-field at oblique angles with respect to the surface will significantly enhance the magnetization precession experiments. Remarkably, the observed MOKE signal saturates at 20% of the absolute value, whereas the simulations show full demagnetization. This behavior will be investigated further by building a two-pulse excitation experiment. This may also allow for coherent control of the magnetization precession.

Bibliography

- [1] “Festkörperphysik. Von Rudolf Gross und Achim Marx”, *Physik in unserer Zeit* **44**, <https://doi.org/10.1002/piuz.201390075> (2013).
- [2] E. Beaurepaire, J.-C. Merle, A. Daunois, and J.-Y. Bigot, “Ultrafast Spin Dynamics in Ferromagnetic Nickel”, *Phys. Rev. Lett.* **76**, 4250–4253 (1996).
- [3] B. Koopmans, G. Malinowski, F. Dalla Longa, D. Steiauf, M. Fähnle, T. Roth, M. Cinchetti, and M. Aeschlimann, “Explaining the paradoxical diversity of ultrafast laser-induced demagnetization”, *Nature Materials* **9**, 259–265 (2010).
- [4] V. N. Kats, T. L. Linnik, A. S. Salasyuk, A. W. Rushforth, M. Wang, P. Wadley, A. V. Akimov, S. A. Cavill, V. Holy, A. M. Kalashnikova, and A. V. Scherbakov, “Ultrafast changes of magnetic anisotropy driven by laser-generated coherent and noncoherent phonons in metallic films”, *Phys. Rev. B* **93**, 214422 (2016).
- [5] A. Eschenlohr, M. Battiato, P. Maldonado, N. Pontius, T. Kachel, K. Holldack, R. Mitzner, A. Föhlisch, P. M. Oppeneer, and C. Stamm, “Ultrafast spin transport as key to femtosecond demagnetization”, *Nature Materials* **12**, 332–336 (2013).
- [6] M. Borchert, C. von Korff Schmising, D. Schick, D. Engel, S. Sharma, and S. Eisebitt, *Manipulation of ultrafast demagnetization dynamics by optically induced intersite spin transfer in magnetic compounds with distinct density of states*, 2020.
- [7] J.-E. Pudell, M. Mattern, M. Hehn, G. Malinowski, M. Herzog, and M. Bargheer, “Heat Transport without Heating?—An Ultrafast X-Ray Perspective into a Metal Heterostructure”, *Advanced Functional Materials* **30**, 2004555 (2020).
- [8] J. Pudell, A. A. Maznev, M. Herzog, M. Kronseder, C. H. Back, G. Malinowski, A. von Reppert, and M. Bargheer, “Layer specific observation of slow thermal equilibration in ultrathin metallic nanostructures by femtosecond X-ray diffraction”, *Nature Communications* **9**, 3335 (2018).
- [9] M. Faraday, “I. Experimental researches in electricity.—Nineteenth series”, *Philosophical Transactions of the Royal Society of London* **136**, 1–20 (1846).
- [10] J. K. LL.D., “XLIII. On rotation of the plane of polarization by reflection from the pole of a magnet”, *The London, Edinburgh, and Dublin Philosophical Magazine and Journal of Science* **3**, 321–343 (1877).
- [11] T. Haider, “A Review of Magneto-Optic Effects and Its Application”, *International Journal of Electromagnetics and Applications* **7**, 17–24 (2017).
- [12] L. Willig, “Ultrafast Magneto-Optical Studies of Remagnetisation Dynamics in Transition Metals”, PhD thesis (University of Potsdam, 2019).
- [13] T. Roth, A. J. Schellekens, S. Alebrand, O. Schmitt, D. Steil, B. Koopmans, M. Cinchetti, and M. Aeschlimann, “Temperature Dependence of Laser-Induced Demagnetization in Ni: A Key for Identifying the Underlying Mechanism”, *Phys. Rev. X* **2**, 021006 (2012).
- [14] J. M. D. Coey, *Magnetism and Magnetic Materials* - (Cambridge University Press, Cambridge, 2010).

- [15] W. Nolting, *Grundkurs Theoretische Physik 5/1: Quantenmechanik - Grundlagen*, 8th ed., Springer-Lehrbuch (Springer Spektrum, 2013).
- [16] T. Gilbert, "A Lagrangian Formulation of the Gyromagnetic Equation of the Magnetization Field", *Physical Review D* **100**, 1243 (1955).
- [17] U. Atxitia, O. Chubykalo-Fesenko, N. Kazantseva, D. Hinzke, U. Nowak, and R. W. Chantrell, "Micromagnetic modeling of laser-induced magnetization dynamics using the Landau-Lifshitz-Bloch equation", *Applied Physics Letters* **91**, 232507 (2007).
- [18] U. Atxitia, D. Hinzke, and U. Nowak, "Fundamentals and applications of the Landau-Lifshitz-Bloch equation", *Journal of Physics D: Applied Physics* **50**, 033003 (2016).
- [19] K. Ohta and H. Ishida, "Matrix formalism for calculation of the light beam intensity in stratified multilayered films, and its use in the analysis of emission spectra", *Appl. Opt.* **29**, 2466–2473 (1990).
- [20] L. Le Guyader, A. Kleibert, F. Nolting, L. Joly, P. M. Derlet, R. V. Pisarev, A. Kirilyuk, T. Rasing, and A. V. Kimel, "Dynamics of laser-induced spin reorientation in Co/SmFeO₃ heterostructure", *Phys. Rev. B* **87**, 054437 (2013).
- [21] D. Schick, "udkm1Dsim – a Python toolbox for simulating 1D ultrafast dynamics in condensed matter", *Computer Physics Communications* **266**, 108031 (2021).
- [22] J.-W. Kim, M. Vomir, and J.-Y. Bigot, "Ultrafast Magnetoacoustics in Nickel Films", *Phys. Rev. Lett.* **109**, 166601 (2012).
- [23] H. J. McSkimin, "Measurement of Elastic Constants at Low Temperatures by Means of Ultrasonic Waves—Data for Silicon and Germanium Single Crystals, and for Fused Silica", *Journal of Applied Physics* **24**, 988–997 (1953).
- [24] P. B. Johnson and R. W. Christy, "Optical constants of transition metals: Ti, V, Cr, Mn, Fe, Co, Ni, and Pd", *Phys. Rev. B* **9**, 5056–5070 (1974).
- [25] W. S. M. Werner, K. Glantschnig, and C. Ambrosch-Draxl, "Optical Constants and Inelastic Electron-Scattering Data for 17 Elemental Metals", *Journal of Physical and Chemical Reference Data* **38**, 1013–1092 (2009).
- [26] I. H. Malitson, "Interspecimen Comparison of the Refractive Index of Fused Silica*,†", *J. Opt. Soc. Am.* **55**, 1205–1209 (1965).
- [27] S. Bridges and L. Robinson, "Chapter 5 - Drilled solids calculations", in *A Practical Handbook for Drilling Fluids Processing*, edited by S. Bridges and L. Robinson, Gulf Drilling Guides (Gulf Professional Publishing, 2020), pp. 105–137.
- [28] S. Andersson and L. Dzhavadov, "Thermal conductivity and heat capacity of amorphous SiO₂: pressure and volume dependence", *Journal of Physics: Condensed Matter* **4**, 6209–6216 (1992).
- [29] D. Cheskis, A. Porat, L. Szapiro, O. Potashnik, and S. Bar-Ad, "Saturation of the ultrafast laser-induced demagnetization in nickel", *Phys. Rev. B* **72**, 014437 (2005).
- [30] K. C. Kuiper, G. Malinowski, F. D. Longa, and B. Koopmans, "Nonlocal ultrafast magnetization dynamics in the high fluence limit", *Journal of Applied Physics* **109**, 07D316 (2011).
- [31] K. C. Kuiper, G. Malinowski, F. D. Longa, and B. Koopmans, "Nonlocal ultrafast magnetization dynamics in the high fluence limit", *Journal of Applied Physics* **109**, 07D316 (2011).
- [32] D. Cheskis, A. Porat, L. Szapiro, O. Potashnik, and S. Bar-Ad, "Saturation of the ultrafast laser-induced demagnetization in nickel", *Phys. Rev. B* **72**, 014437 (2005).

-
- [33] M. S. Lucile, “Pulsed laser deposition of substituted thin garnet films for magnonic applications”, PhD thesis (Université Paris-Sud, 2019).
- [34] M. Deb, E. Popova, M. Hehn, N. Keller, S. Petit-Watelot, M. Bargheer, S. Mangin, and G. Malinowski, “Femtosecond Laser-Excitation-Driven High Frequency Standing Spin Waves in Nanoscale Dielectric Thin Films of Iron Garnets”, *Phys. Rev. Lett.* **123**, 027202 (2019).
- [35] C. Thomsen, H. T. Grahn, H. J. Maris, and J. Tauc, “Surface generation and detection of phonons by picosecond light pulses”, *Phys. Rev. B* **34**, 4129–4138 (1986).
- [36] A. Bojahr, M. Gohlke, W. Leitenberger, J. Pudell, M. Reinhardt, A. von Reppert, M. Roessle, M. Sander, P. Gaal, and M. Bargheer, “Second Harmonic Generation of Nanoscale Phonon Wave Packets”, *Phys. Rev. Lett.* **115**, 195502 (2015).
- [37] M. van Kampen, C. Jozsa, J. T. Kohlhepp, P. LeClair, L. Lagae, W. J. M. de Jonge, and B. Koopmans, “All-Optical Probe of Coherent Spin Waves”, *Phys. Rev. Lett.* **88**, 227201 (2002).

Declaration of Authorship

I, Fried-Conrad WEBER, declare that this thesis titled, "Light-induced magnetization dynamics in Nickel under different excitation conditions" and the work presented in it are my own. I confirm that:

- This work was done wholly or mainly while in candidature for a research degree at this University.
- Where any part of this thesis has previously been submitted for a degree or any other qualification at this University or any other institution, this has been clearly stated.
- Where I have consulted the published work of others, this is always clearly attributed.
- Where I have quoted from the work of others, the source is always given. With the exception of such quotations, this thesis is entirely my own work.
- I have acknowledged all main sources of help.
- Where the thesis is based on work done by myself jointly with others, I have made clear exactly what was done by others and what I have contributed myself.

Signed:

Date:
